

Mechanisms of Morphing Wall Flow Control by Traveling Waves over an Airfoil

Uchenna E Ogunka,* Amir M Akbarzadeh,† and Iman Borazjani‡
Texas A&M University, College Station, Texas 77840

https://doi.org/10.2514/1.J062449

The main two mechanisms of morphing wall flow control are direct injection of momentum in the streamwise direction and indirect momentum transfer via triggering instabilities. Traveling waves have been shown to perform better than standing waves, probably because they can use both mechanisms. However, the relative importance of the two mechanisms is not known. To differentiate between the mechanisms, a range of parameters (frequency, amplitude, and starting location) at stall (15 deg angle of attack) and poststall (20 deg angle of attack) is tested using wall-resolved large-eddy simulations with a sharp-interface curvilinear immersed boundary method at a low Reynolds number of Re = 50,000 over a NACA0018 airfoil. The results of the simulations demonstrate that the flow is reattached within a range of nondimensional frequencies, actuation amplitudes, and starting locations of oscillation at the stall and poststall angles of attack. Significant lift enhancement and drag reduction are also observed within these ranges. The nondimensional frequency range at which the flow is reattached is found to be similar to the dominant nondimensional frequencies of leading-edge vortex shedding of the unactuated airfoil. These indicate that the indirect transfer of momentum is the dominant mechanism because direct injection of momentum increases with the increase of amplitude and frequency; that is, separation should reduce as they increase. Nevertheless, direct injection of momentum improves the performance relative to pure excitations of standing waves when instabilities are triggered.

Nomenclature

a = maximum amplitude of oscillation

 a^* = nondimensional amplitude of oscillation; a/L

C = wave speed; λf

 C^* = nondimensional wave speed; C/U

 $\bar{C_D}$ = mean drag coefficient; $\bar{F_D}/0.5\rho U^2 L$

 \bar{C}_f = mean skin-friction coefficient

 $\vec{C_L}$ = mean lift coefficient; $\vec{F_L}/0.5\rho U^2 L$

 \bar{C}_{n} = mean pressure coefficient

 \bar{F}_D = mean drag force per airfoil unit span acting along the x

 $\vec{F_L}$ = mean lift force per airfoil unit span acting along the y direction

f = frequency

 f^* = nondimensional frequency; fL/Uh = displacement of the suction side

L = chord length of the airfoil P = fluid pressure

P = fluid pressurep = p value of statistical two-sample t test

 $Re = \text{Reynolds number; } UL/\nu$ s = airfoil span length; 0.1L

t = time

U = freestream velocity

 X_0 = nondimensional starting location of oscillation on airfoil

suction side along streamwise direction; X/L

 $\delta t = \text{time step}$ $\lambda = \text{wavelength}$

 λ^* = nondimensional wavelength; λ/L

Presented as Paper 2021-2005 at the AIAA SciTech Forum, Virtual, January 19–21, 2021 and Paper 2022-1948 at the AIAA SciTech Forum, San Diego, CA, January 3–7, 2022; received 14 September 2022; revision received 6 November 2022; accepted for publication 7 November 2022; published online 29 December 2022. Copyright © 2022 by the American Institute of Aeronautics and Astronautics, Inc. All rights reserved. All requests for copying and permission to reprint should be submitted to CCC at www.copyright.com; employ the eISSN 1533-385X to initiate your request. See also AIAA Rights and Permissions www.aiaa.org/randp.

*Ph.D. Candidate, J. Mike Walker '66 Department of Mechanical Engineering.

[†]Postdoctoral Researcher, J. Mike Walker '66 Department of Mechanical Engineering.

[‡]Associate Professor, J. Mike Walker '66 Department of Mechanical Engineering.

 ν = kinematic viscosity ρ = fluid density

I. Introduction

F LOW control at low Reynolds numbers (Re < 500,000) [1] is of particular interest to migra size 1.11 - 500particular interest to micro air vehicles [2] and unmanned aerial vehicles [3]. At low Reynolds numbers, a laminar boundary layer forms on the suction (upper) side of the airfoil, which may separate and fail to reattach when the angle of attack (AOA) surpasses the airfoil's stall angle [4-6]. Boundary-layer separation reduces the aerodynamic performance (increases drag and reduce lift) of the aforementioned aerial vehicles. Therefore, flow control techniques have been adopted to reduce and even eliminate flow separation [7]. Flow control techniques can be classified based on the mechanism of reattachment: 1) direct injection of momentum in the streamwise direction into the boundary layer, e.g., suction and blowing [8-12]; and 2) indirect transfer of momentum by the triggering of instabilities passively, e.g., surface roughness bumps [13], vortex generators [14,15], or actively through periodic excitation [16]. Periodic excitations such as actuators [6,17,18], synthetic jets [19,20], and acoustic excitations [21] trigger an inherent flow instability, e.g., Tollmien-Schlichting transitioning a laminar boundary layer into a turbulent one [22] or accelerating the formation of large coherent structures (LCSs) in the boundary layer via the triggering of Kelvin-Helmholtz (K-H) instability [6], thereby increasing the mixing of high-momentum fluid of the separated shear layer with the low-momentum fluid of the reverse flow zone.

Surface actuation is an energy-efficient technique that makes use of light inexpensive piezoelectric actuators [23,24]. Piezoelectric actuators are attached along the upper surface (suction side) of the airfoil where they interact with the near-wall boundary layer. These piezoelectric actuators typically create a standing wave [6,17,18] that increases the fluid's kinetic energy at the near wall by periodic excitation and have been shown to reduce flow separation [6,17,18,25,26]. Compared to standing waves, traveling waves can be created via piezoelectric actuators, but not as easily as standing waves [27]. Backward-traveling waves are typically used by aquatic animals to swim forward [28–30], which have been shown to keep the flow attached to the swimmer's body [31,32]. Backward-traveling (opposite to the airfoil's forward motion) waves might perform better than standing waves because they can directly inject momentum into the boundary layer in the streamwise direction as well as trigger instabilities (amplification of the K-H instability, hence regulating the generation of LCSs). Akbarzadeh and Borazjani [33] found that

traveling waves outperform standing waves in controlling flow separation over an airfoil. However, the relative importance of the mechanisms (direct injection of momentum versus the indirect one) is still unknown.

The axial force generated by a traveling wave is of order $\mathcal{O}\left\{a^{*2}[f^*-(1/\lambda^*)]^2\right\}$ [34], which is derived based on Lighthill's elongated body theory (EBT) [35], where f^* is the nondimensional frequency ($f^* = fL/U$, where f denotes the frequency, U denotes the freestream velocity, and L denotes the airfoil chord length), a^* is the nondimensional amplitude ($a^* = a/L$, where a denotes the amplitude), and λ^* is the nondimensional wavelength ($\lambda^* = \lambda/L$, where λ denotes the wavelength). If the direct injection of momentum is the main mechanism, then increasing the frequency and amplitude should reduce flow separation. However, if triggering is dominant, flow separation might not decrease if the frequency and amplitude increase; i.e., there might be an upper bound limit on the frequency and amplitude [17,18], and the location of excitation may be important [6,21]. Previous work from our group investigated the roles of frequency and amplitude in traveling wave flow control of a turbulent channel [36], an inclined plate [34], and a NACA0018 airfoil at nearstall (AOA = 10 deg) [37] and stall (AOA = 15 deg) [33] angles of attack. They observed that flow separation reduced as the frequency increased. They also observed that increasing the frequency increased the lift enhancement and drag reduction of the airfoil [33]. However, the maximum frequency tested was $f^* = 8.0$ [33], and higher frequencies ($f^* > 8.0$) need to be explored. Similarly, they observed that the range of amplitude, $0.001 \le a^* \le 0.002$, significantly reduced the flow separation, increased the lift, and reduced the drag over the airfoil [33,37]. However, the amplitudes tested are higher than the range of amplitudes of experimental traveling wave oscillations that can be generated from piezoelectric actuators $(2 \times 10^{-3} > a^* > 6 \times 10^{-5})$ [38,39]. Therefore, lower amplitudes and higher frequencies of traveling wave oscillations still need to

The goal of this study is to identify the relative importance of the two mechanisms (direct injection vs indirect momentum transfer) for traveling waves, thereby obtaining the range of parameters that will achieve optimal flow control for the initial design of traveling wave actuators. To attain this goal, the wave parameters (frequency f^* , amplitude a^* , and excitation location X_0) at the stall and poststall angles of attack are varied in our numerical simulations to see if they monotonically reduce separation (then direct injection of streamwise momentum is dominant) or if there is a bound for the parameters (and then indirect momentum transfer will be dominant). A comparison of the numerical simulation results of the traveling wave morphing against standing wave morphing is also performed. This paper is organized as follows: The governing equations, computational mesh, and numerical methods for wallresolved large-eddy simulations (LESs) are described in Sec. II. The lift and drag coefficient of the NACA0018 airfoil for different frequencies and amplitudes are compared against an unactuated (baseline) NACA0018 airfoil (Sec. III). The observed trends are explained by visualizing the flowfield (Sec. III). A discussion on the results and their comparison with previous work are provided in Sec. IV. Finally, the results are discussed and the conclusions are reported in Sec. V.

II. Method

Numerical simulations are performed for a NACA0018 airfoil near the stall and poststall angles of attack (AOA = 15-20 deg) at which the flow starts to separate from the leading edge, and a large reverse flow is generated on the suction side of the airfoil. The structure of the simulation and the numerical method employed for solving the problem are similar to previous publications [33,37,40,41]. The freestream velocity U and the airfoil chord length L are, respectively, the characteristic velocity and length; and $Re = UL/\nu = 50,000$, where ν is the kinematic viscosity. The airfoil geometry and fluid mesh are shown in Fig. 1. The suction side of the airfoil undergoes a backward-traveling (opposite to the airfoil's forward motion) wave deformation. To calculate the new location of the suction side of the airfoil under motion in the original Cartesian frame (x, y, z), a local frame (X, Y, Z) is defined; i.e. its origin is at the leading edge and is rotated by the angle of attack (Fig. 1b). The backward-traveling wave oscillation [h(X, t)] prescribed along the Y direction is

$$h^*(X,t) = a^*(X)\sin(2\pi(f^*t^* - X^*/\lambda^*)) \tag{1}$$

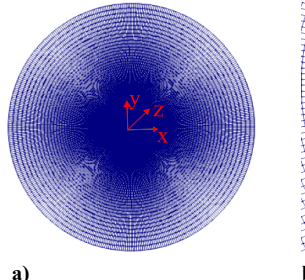
Moreover, the equation of the standing wave oscillation, prescribed along the *Y* direction is

$$h^*(X,t) = a^*(X)\sin(2\pi f^*t^*)\sin(2\pi X^*/\lambda^*)$$
 (2)

where $h^* = h/L$ is the nondimensional displacement of the suction side, $f^* = fL/U$ is the nondimensional frequency, $\lambda^* = \lambda/L$ is the nondimensional wavelength, $t^* = tU/L$ is the nondimensional time unit, $X^* = X/L$ is the nondimensional streamwise length that starts from the leading edge, $X_0 = X/L$ is the starting location of oscillation of the actuator, and $a^*(X) = a(X)/L$ is the amplitude of the wave. The amplitude $a^*(X)$ remains constant and equal to its maximum value a^*_{\max} from $X = (X_0 + 0.05)L$ to X = 0.8L and decreases linearly toward the leading and trailing edges, as illustrated in Fig. 2. The backward-traveling wave propagates with a nondimensional wave speed of $C^* = \lambda^* f^*$ from the leading edge toward the trailing edge. Here, the parameters with the asterisk (*) symbol are non-dimensional.

The governing equations for the flow are the unsteady, three-dimensional, incompressible, filtered Navier–Stokes, and continuity equations. The governing equations are discretized via a second-order central scheme and integrated in time using a second-order fractional-step methodology [42,43]. The momentum equations are solved with a Newton–Krylov method with an approximate analytical Jacobian solver [44], and the pressure Poisson equation is solved using a generalized minimal residual (GMRES) solver with a multigrid preconditioner [42,43].

The moving boundaries are handled using the sharp curvilinear immersed boundary method (CURVIB), which was explained in previous publications [42,43,45]. In this method, the background mesh is fixed and the airfoil surface motion [i.e., the prescribed surface motion given in Eq. (1) for traveling wave motion and Eq. (2) for standing wave motion] discretized using a triangular mesh is set as a sharp-interface immersed boundary over the background mesh (Fig. 3). The grid nodes found inside the immersed boundary (moving boundary) are classified as solid nodes. The solid nodes are blanked out, whereas the velocities of the fluid points (nodes)



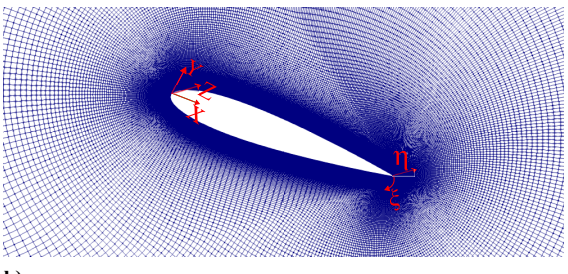


Fig. 1 Representations of a) computational O-grid mesh domain and b) simulation setup with O-grid mesh around NACA0018 airfoil.

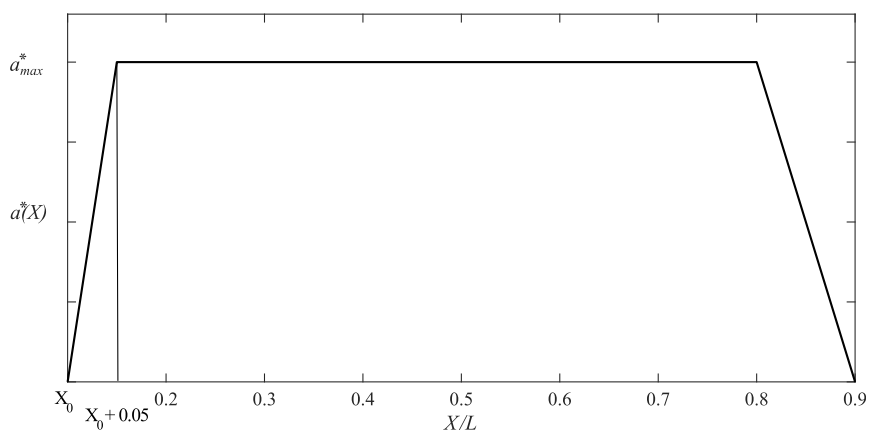


Fig. 2 Amplitude as a function of chord length of airfoil's suction side with starting location of oscillation of $X_0 = 0.1$.

adjacent to the moving boundaries (immersed nodes) are reconstructed using an interpolation along the surface normal. The classification of the domain into solid, immersed, and fluid nodes is performed by a ray tracing algorithm [43]. A no-slip boundary condition is prescribed at the moving boundaries. The CURVIB method is validated for flows with moving boundaries [43] and has been applied in simulations involving turbulent flow [46] and biological flows such as aquatic locomotion [47–49], cardiovascular flows [43,50–52], and aneurysm blood flow [53,54]

The turbulent flow is modeled using a large-eddy simulation method. Here, a dynamic subgrid-scale model [55], without triggering, is used to compute the subgrid stress tensor because previous studies [56,57] have shown that subgrid-scale models are suitable for modeling transitional turbulent flows. The flow is fully separated in the unactuated case such that it automatically becomes a turbulent flow. The LES was validated extensively for wall-bounded flows in previous studies [34,36,48]. The LES of the fully developed turbulent channel [36] confirmed that our LES can resolve the mean flow and turbulent statistics of turbulent boundary layers. Moreover, the LES is validated for transitional and turbulent flows over bluff bodies such as inclined plates, oscillating airfoils [34], and circular cylinders [48]. The LES of the unactuated case, in which the flow is separated, was performed until the quasi-steady state was reached. Also, the turbulence kinetic energy (equal to $\langle u_i^2 \rangle / 2$; <> is the volume average in the domain, and u_i (i = 1, 2, 3) is the *i*th component of the velocity) in the quasi-steady-state domain does not vary significantly in time. The LESs of the actuated cases are initialized by the LES of the unactuated case. The details of our LES modeling and its validation can be found in previous studies [36,45].

The computational mesh is the same as in a previous study [33]. The grid adopted for the fluid domain is an O grid (Fig. 1a) generated in curvilinear coordinates (ξ, η, ζ) , where ξ is parallel to the airfoil surface and η is normal to the airfoil surface. The resolution of the grid is $421 \times 281 \times 21$ in the (ξ, η, ζ) direction. The grid is extruded in the ζ direction

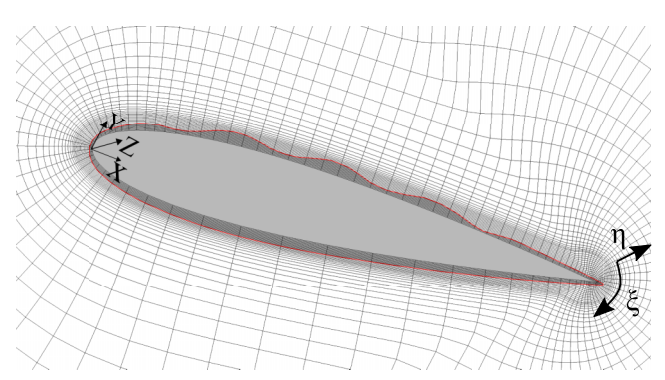


Fig. 3 Oscillating airfoil surface (red line) inside O-grid mesh. Adapted from Ref. [33] and reprinted with permission.

for 0.1L (spanwise length) to generate a three-dimensional domain. The spanwise length of the computational domain is selected to be 0.1L in order to minimize computational cost. This spanwise domain length has been shown to be sufficiently suitable for prior simulations involving active flow control via periodic excitations over airfoils at high angles of attack and low Reynolds numbers [33,37]. For a thorough description of the sensitivity of the computational domain spanwise length and grid, the reader is referred to the previous studies of Akbarzadeh and Borazjani [34,37]. Furthermore, a grid refinement study for the LESs of flow over a baseline airfoil at a 15 deg angle of attack is provided in the Appendix. The approximate radius of the O-grid mesh shown in Fig. 1a is 15L. A zoomed-in view of the mesh near the airfoil is shown in Fig. 1b. The boundary conditions along ξ and ζ are periodic. On the outer boundary η , the upstream is characterized by an inlet velocity $(u_x = U)$ at x < 0, whereas the downstream is characterized with a Neumann boundary condition with a mass flux correction at x > 0. To resolve the boundary layer at AOA = 15 deg, the grid resolution is maintained constant at 0.0003L along the η direction near the airfoil surface that corresponds to a wall unit spacing of $\eta^+ = 0.9$ ($\eta^+ = \delta_\eta u_\tau / \nu$; δ_η is the normal distance between the first fluid node and the wall surface, and u_{τ} is the friction velocity), whereas for AOA = 20 deg, the grid resolution is kept constant at 0.00019Lalong the η direction with a wall unit spacing of $\eta^+ = 0.5$. This was chosen to ensure that η^+ < 1.0 is preserved as the airfoil surface moves with the prescribed motion [Eq. (1) or Eq. (2)] during the simulation. Note that the grid resolution is not fine enough to resolve amplitudes less than the minimum grid spacing of 0.0003L (AOA = 15 deg) and 0.00019L (AOA = 20 deg). Although the amplitude less than the minimum grid spacing is not resolved, the velocity of the surface is resolved because of the sharp-interface nature of our immersed boundary method. The CURVIB method imposes the surface velocity (at the exact location of the interface) as the boundary condition for the flow without diffusing it over several grid nodes. The grid spacing is constant until $\eta = 0.022$; then, it increases with a hyperbolic function to the boundaries. The minimum grid spacing along the airfoil circumference and span is equivalent to wall unit spacings of $\xi_{\min}^{+}=1.3$ and $\zeta_{\min}^{+}=13$, respectively, similar to a previous study [33]. The time step is 0.001L/U for the baseline (unactuated) case and actuated cases at 15 deg and 0.0003L/U for the simulations at 20 deg, corresponding to the Courant–Friedrichs–Lewy (CFL) number of $U\delta t/\Delta x \leq 0.5$. Each cycle of the actuated case consists of 500 to 2000 time steps, depending on the frequency of the oscillations. It has been chosen such that CFL < 0.35.

To verify the quality of the LES, the LES index quality (LESIQ) proposed by Celik et al. [58] is used. Celik et al. [58] recommends at least 80% for good LES quality. The LES index quality is calculated near the unactuated airfoil centerline (y=0.3L), which has the highest turbulence intensity in the wake of the airfoil (x=1.5L and x=2.5L) for both grids. The LESIQ was approximately 80%, suggesting that the LES is of good quality.

More details on the simulation setup, grid sensitivity study, and validation can be found in previous studies [33,37].

To quantify the aerodynamic performance of the NACA0018 airfoil, the mean lift coefficient

$$C_L = \frac{\bar{F_L}}{0.5\rho U^2 L}$$

the mean drag coefficient

$$C_D = \frac{\bar{F_D}}{0.5\rho U^2 L}$$

the mean pressure coefficient

$$C_f = \left(\frac{2}{Re}\right) \left(\frac{\partial u_x^*}{\partial y^*}\right)$$

the mean power coefficient

$$C_{po} = \frac{1}{0.5\rho U^3 A t^*} \int_{t^*} \left(\int_A -P n_Y \dot{h} \, dA \right) dt$$

and the standard deviation σ are computed by averaging at least 10 cycles for the actuated cases and at least 40 nondimensional time units $(t^* = tU/L)$ reported in Table 1:

$$\frac{\partial u_x^*}{\partial y^*} = \frac{\partial u_x^*}{\partial \xi} \frac{\partial \xi}{\partial y^*} + \frac{\partial u_x^*}{\partial \eta^*} \frac{\partial \eta}{\partial y^*}$$

is the velocity gradient in curvilinear coordinates, \bar{P} is the mean fluid pressure, \bar{F}_L is the mean force per unit airfoil span acting along the y direction, \bar{F}_D is the mean force per unit airfoil span acting along the x direction, ρ is the fluid density, \dot{h} is the velocity of the surface oscillation in the Y direction, n_Y is the surface normal component in the Y direction, dA is the area of the surface element, and A is the area of the actuated surface of the airfoil's suction (upper) side. Here, the overbar denotes time-averaged values. The mean pressure coefficient is computed with the reference pressure (zero pressure) located at the trailing edge (X, Y = L, 0). The top parts of the \bar{C}_p and \bar{C}_f profile plots represent the suction surface of the airfoil, whereas the pressure surface is represented by the bottom parts of the profiles. In this study, all mean parameters (e.g., \bar{C}_p) are time

averaged along the span of the airfoil as well because the airfoil is two-dimensional (2-D). The separation and reattachment locations on the suction side of the airfoil are defined where $\bar{C}_f < 0$ and $\bar{C}_f > 0$, respectively.

The statistical two-sample t test was employed to compare the mean C_L and C_D of the NACA0018 airfoil cases. The datasets of two samples at different f^* , a^* , and X_0 were compared with each other and the unactuated case. The statistical two-sample t test determines if the means of two datasets are significantly different from each other (p < 0.05) or the means of the two datasets are statistically similar (p > 0.05).

III. Results

To identify the dominant mechanism of flow control, the effects of the wave parameters (frequency f^* , amplitude a^* , and starting location of oscillations X_0) of the backward-traveling wave on the aerodynamic performance of the NACA0018 airfoil at AOA = 15–20 deg are investigated by comparing the mean coefficients of lift and drag with the unactuated airfoil. Moreover, the mean spanwise-averaged coefficients of the pressure and skin friction are examined to better observe the enhancement of the lift coefficient and the location of the separation and reattachment on the upper surface of the airfoil, respectively. Lastly, the contours of the instantaneous spanwise vorticity and the three-dimensional isosurface of the Q criterion of the unactuated and actuated airfoils are visualized. As stated in Sec. II, the data presented in this Sec. III are collected from the final 10 cycles for both the unactuated and actuated cases.

To obtain the bounds for frequency, the leading-edge vortex shedding frequency is analyzed via the fast Fourier transform for the unactuated airfoil at a 15 deg AOA. Figure 4 shows the power spectrum density of the frequency domain for the unactuated airfoil. The spectrum is computed by spectrum analysis of the streamwise velocity u_x for a total nondimensional time of $t^* = 220$ at a point near the leading edge, i.e., at X = 0.086L and Y = 0.28L with respect to the leading edge (X, Y = 0, 0) (Fig. 1b). The plot indicates the shedding frequency of the shear layer is in the range of $f^* = 6$ to $f^* = 10$. The frequencies of the actuation were kept within the vicinity of the range of the leading-edge vortex shedding frequency. In addition, frequencies outside the leading-edge vortex shedding frequency range were investigated. Specifically, the frequencies tested in this study were $f^* = 4, 8, 10, 12, 16$, and 20. In addition to the frequency, the amplitude and starting location of the oscillations were also varied. The

Table 1 Case studies including unactuated airfoil as well as backward-traveling and standing wave actuations with different frequencies f^* , amplitudes a^* , and starting locations of oscillation X_0^a

_											_	
Case	Wave type	f^*	a*	X_0	<i>C</i> *	C_L	C_D	σ_{C_L}	σ_{C_D}	AOA, deg	C_{po}	$\sigma_{C_{po}}$
1	Unactuated	0.0	0.0	0.0		0.676	0.279	0.191	0.047	15	0.0	0.0
2	Backward-traveling wave	4.0	0.00006	0.1	1.76	0.70	0.284	0.246	0.067	15	0.0000034	0.0000026
3	Backward-traveling wave	10.0	0.00006	0.1	4.40	0.75	0.301	0.181	0.043	15	0.0000080	0.0000059
4	Backward-traveling wave	20.0	0.00006	0.1	8.80	0.63	0.283	0.206	0.043	15	0.000082	0.000012
5	Backward-traveling wave	8.0	0.0005	0.1	3.52	0.76	0.253	0.160	0.038	15	0.00010	0.000040
6	Backward-traveling wave	4.0	0.001	0.1	1.76	0.69	0.262	0.185	0.055	15	0.000052	0.000048
7	Backward-traveling wave		0.001	0.0	3.52	0.90	0.090	0.140	0.042	15	0.00025	0.00010
8	Backward-traveling wave $(X/L \in (X_0, 0.9))$		0.001	0.1	3.52	0.89	0.090	0.151	0.035	15	0.00016	0.000083
9	Backward-traveling wave		0.001	0.2	3.52	0.70	0.261	0.160	0.038	15	0.000040	0.000074
10	Backward-traveling wave	12.0	0.001	0.1	5.28	0.87	0.098	0.293	0.071	15	0.00023	0.00013
11	Backward-traveling wave	16.0	0.001	0.1	7.04	0.67	0.247	0.506	0.127	15	0.00040	0.00024
12 ^b	Backward-traveling wave	8.0	0.002	0.1	3.52	0.92	0.090	0.170	0.040	15	0.00027	0.00019
13	Backward-traveling wave	8.0	0.004	0.1	3.52	0.86	0.100	0.476	0.117	15	0.00057	0.00047
14	Standing wave $(X/L \in (X_0, 0.9))$	8.0	0.001	0.1	3.52	0.82	0.106	0.160	0.036	15	0.00024	0.00018
14b	Backward-traveling wave $(X/L \in (X_0, 0.2))$	8.0	0.001	0.1	3.52	0.90	0.090	0.135	0.012	15	0.00005	0.00003
15	Unactuated	0.0	0	0		0.70	0.308	0.170	0.057	20	0.0	0.0
16	Backward-traveling wave	4.0	0.001	0.1	1.76	0.69	0.26	0.140	0.052	20	0.000072	0.000046
17	Backward-traveling wave	8.0	0.001	0.1	3.52	0.87	0.17	0.143	0.048	20	0.00015	0.000090
18	Backward-traveling wave	10.0	0.001	0.1	4.40	0.86	0.17	0.196	0.069	20	0.00018	0.00010
19	Backward-traveling wave	16.0	0.001	0.1	7.04	0.69	0.28	0.297	0.116	20	0.00031	0.00013

 $^{{}^{}a}C_{L}$, C_{D} , and C_{po} are the lift, drag, and power coefficients, respectively; and $\sigma_{C_{L}}$, $\sigma_{C_{D}}$, and $\sigma_{C_{\infty}}$ are the standard deviations of the lift, drag, and power coefficients.

^bCase 12 is from Ref. [33].

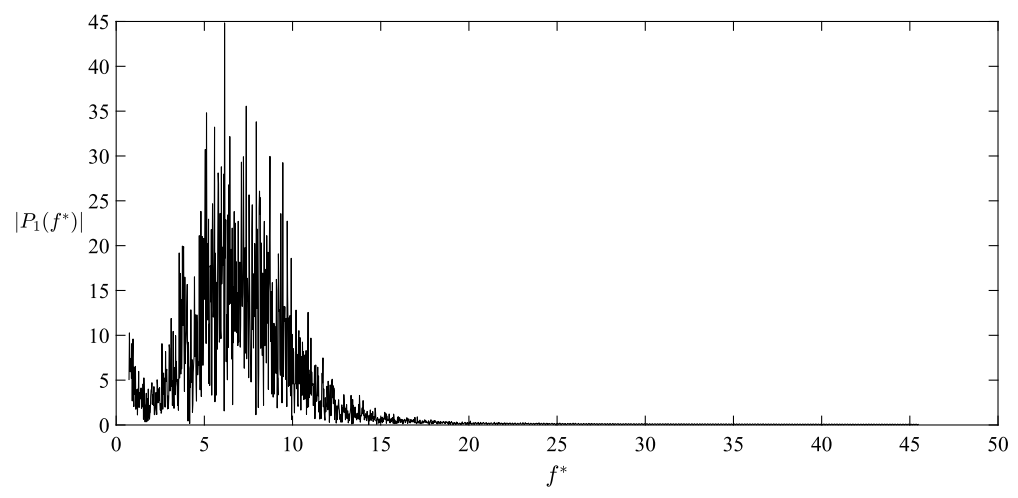


Fig. 4 Power spectrum density plot of velocity P_1 in the frequency domain for unactuated airfoil at AOA = 15 deg at leading edge.

amplitude was varied between $a^* = 0.0006$ and $a^* = 0.004$, which covers the range that traveling waves have generated experimentally [38,39]. The separation point of the unactuated airfoil at AOA = 15 deg is at X/L = 0.04. Therefore, the range for the starting location of the actuation was selected to be $0.0 \le X_0 \le 0.2$ ($X_0 = X/L$). The wavelength is kept constant at $\lambda^* = 0.44$, which is the same as the traveling waves generated experimentally [38,39].

The wave parameters for the studied cases are presented in Table 1 along with the average lift, power, and drag coefficients. Moreover, the standard deviation is reported in Table 1 to investigate the significance of the variation of the mean forces and power with respect to the baseline (unactuated) case. Note that the error bars, which represent the standard deviation, are included in the plots of the average lift, drag, pressure, and skin-friction coefficients. The first case is an unactuated (baseline) airfoil, and cases 2-13 are actuated airfoils with backward-traveling waves with amplitude range of $a^* =$ 0.00006 to $a^* = 0.004$, a frequency range of $f^* = 4$ to $f^* = 20$ (corresponding wave speed range of $C^* = 1.76$ to $C^* = 8.80$), and a starting location range of $X_0 = 0.0$ to $X_0 = 0.2$. Case 14 is an actuated airfoil with standing waves with an amplitude of $a^* = 0.001$ and a frequency of $f^* = 8$. The upper surface of the airfoil in cases 2–14 is actuated from $X/L = X_0 - 0.9$; i.e., the wave oscillations start at $X/L = X_0$ and terminate at X/L = 0.9. Case 14b is an actuated airfoil with backward-traveling waves that begin from X/L = 0.1 and end at X/L = 0.2 (i.e., 10% of the upper surface is actuated). The angle of attack of cases 1-14b is AOA = 15 deg, whereas cases 15-19 have an angle of attack of AOA = 20 deg. Cases 2–4 have the lowest amplitude ($a^* = 0.00006$), with the other cases having significantly higher amplitudes, e.g., $a^* \ge 0.0005$. From Table 1, it can be observed that the mean power for these oscillations is small as compared with the power loss due to drag $(U \times C_D)$. In Sec. III.A, the effects of frequency on the aerodynamic performance (mean lift coefficient, mean drag coefficient, mean spanwise pressure coefficient, and mean spanwise skin-friction coefficient) are discussed by comparing cases 1-4, 6, 8, 10, and 11 for stall (AOA = 15 deg) and cases 15-19 for poststall (AOA = 20 deg), in which only the frequency is varied and the rest of the parameters are the same. Also, the effects of the amplitude and starting location of oscillation on the aerodynamic performance (mean lift coefficient, mean drag coefficient, mean spanwise pressure coefficient, and mean spanwise skin-friction coefficient) are discussed by comparing cases 5, 8, 12–13 in Sec. III.B, and cases 7–9 in Sec. III.C, respectively. The flowfield around the airfoil, detailing the effects of different actuations on the vorticity, is discussed in Sec. III.D.

A. Effect of Frequency at Stall and Poststall

The mean C_L and C_D (symbols) and their standard deviations (error bars) are plotted for different actuation frequencies f^* at stall (AOA = 15 deg) and poststall (AOA = 20 deg) in Figs. 5 and 6, respectively. Note that the error bars represent the standard deviation of the mean C_L and C_D for the time cycle duration. As can be seen from Figs. 5 and 6 for the low-amplitude ($a^* = 0.00006$) actuations at stall (represented by \square), the increase of the nondimensional frequency to $f^* = 4$, $f^* = 10$, and $f^* = 20$ leads to small negligible percentage changes in C_L and C_D as compared to the unactuated case.

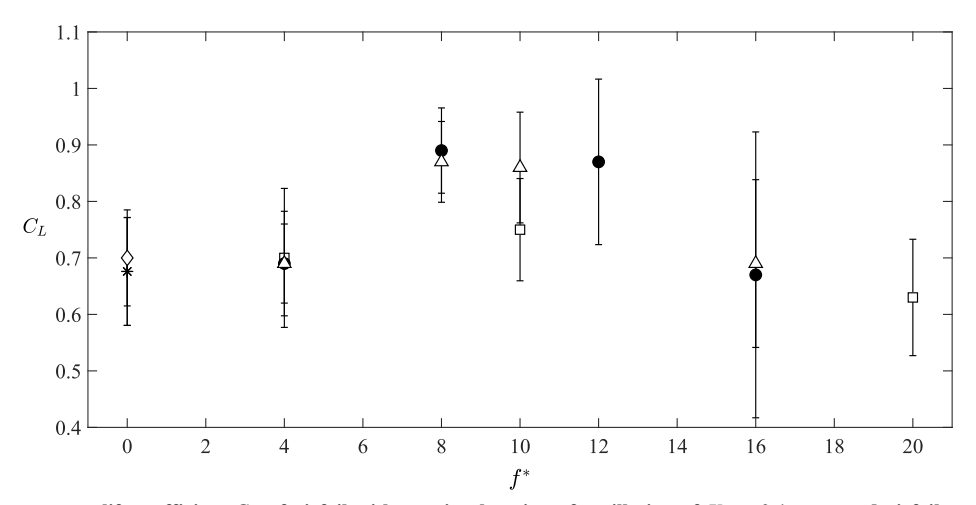


Fig. 5 Effect of frequency on lift coefficient C_L of airfoil with starting location of oscillation of $X_0 = 0.1$: actuated airfoil at AOA = 15 deg and amplitudes of $a^* = 0.00006$ (squares) and $a^* = 0.001$ (circles); actuated airfoil at AOA = 20 deg and amplitude of $a^* = 0.001$ (triangles); and unactuated case for AOA = 15 deg (asterisks) and AOA = 20 deg (diamonds).

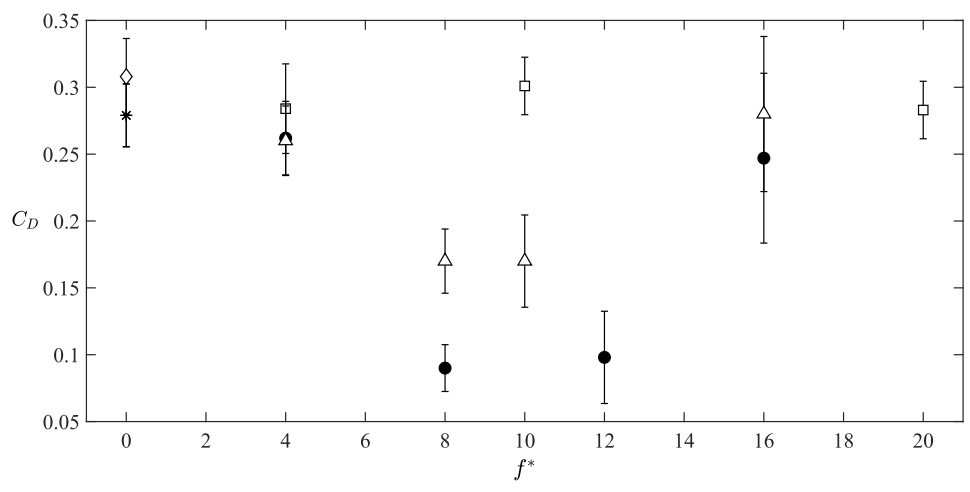


Fig. 6 Effect of frequency on drag coefficient C_D of airfoil with starting location of oscillation of $X_0 = 0.1$: same designations as Fig. 5.

However, these increases/decreases are not statistically significant (p>0.05); i.e., C_L and C_D for actuated and unactuated cases are similar. This indicates that the actuation with a low amplitude of $a^*=0.00006$ at any frequency is insignificant. To investigate further, the amplitude of actuations is increased to $a^*=0.001$ (represented by solid circles; •) in Figs. 5 and 6. For $a^*=0.001$, there are small insignificant percentage deviations (p>0.05) in C_L and C_D at $f^*=4$ and $f^*=16$ as compared to the unactuated case, i.e., statistically similar to the unactuated case. When the nondimensional frequency changes to $f^*=8$ in case 7, however, C_L significantly increases by 32% (p<0.05) and C_D significantly decreases by 68% (p<0.05) as compared to the unactuated case. Increasing the frequency to $f^*=12$ in case 8, C_L decreases and C_D increases, but both remain statistically similar to case 8 (p>0.05) while still significantly (p<0.05) higher and lower, respectively, than the unactuated case.

A similar trend is observed at poststall, where the angle of attack is increased to AOA = 20 deg (represented by triangles; Δ) in Figs. 5 and 6. At poststall (AOA = 20 deg), C_L and C_D remain statistically similar (p > 0.05) to the unactuated case (case 15) at $f^* = 4$ (case 16) and $f^* = 16$ (case 19). Changing the frequencies to $f^* = 8$ (case 17) and $f^* = 10$ (case 18), there is a significant increase in C_L by 23% (p < 0.05) and a significant reduction of 54% (p < 0.05) in C_D . Based on the aforementioned information, there is a range of frequencies f^* at both stall (AOA = 15 deg) and poststall (AOA = 20 deg) at which significant lift enhancement and drag reduction are observed for $a^* = 0.001$ actuations. This frequency range where the maximum lift enhancement and drag reduction were observed is similar to the range of the leading-edge vortex shedding frequency observed in Fig. 4. This suggests that backward-traveling wave oscillations with a frequency f^* range equal to or closely equal to the leading-edge vortex shedding frequency range are needed to suppress stall and improve the aerodynamic performance of the airfoil.

The observed trends of lift and drag coefficients can better be explained by the distribution of the time-averaged pressure coefficient \bar{C}_p and the time-averaged skin-friction coefficient \bar{C}_f around the airfoil, which are plotted in Figs. 7 and 8, respectively. The top parts of the \bar{C}_p and \bar{C}_f plots represent the suction (upper) surfaces of the airfoil, whereas the pressure surfaces are represented by the bottom parts of the profiles. The pressure coefficient profile of the unactuated case depicts a stalled airfoil (at AOA = 15-20 deg) because on the suction side of the unactuated case, \bar{C}_p decreases near the leading edge, peaking at X/L = 0.02. Then, it increases and keeps a flat profile within the range of 0.07 < X/L < 0.8. Applying a low-amplitude $(a^* = 0.00006)$ actuation at AOA = 15 deg (stall), all the pressure profiles are close to the unactuated case, which explains the insignificant C_L and C_D as compared to the unactuated case (Fig. 7a). At $a^* = 0.001$, the C_n plots at $f^* = 4$ and $f^* = 16$ are both similar to the unactuated case (Fig. 7b), which explains the insignificant differences in C_L and C_D as compared to the unactuated case.

However, the \bar{C}_p plots at $f^* = 8$ and $f^* = 12$ are similar to each other but differ significantly from the unactuated case (Fig. 7b). Both experience a higher \bar{C}_p peak near the leading edge at X/L = 0.014 as compared to the unactuated case (Fig. 7b). The significant increase in the pressure peak near the leading edge (Fig. 7b) coincides with the lift C_L enhancement observed at these frequencies ($f^* = 8$ and $f^* = 12$) [6]. From Fig. 7b, the significant rise in the pressure peaks near the leading edge on the airfoil's suction side suggests that the point of separation may have been moved downstream as compared to the unactuated (baseline) case [59]. The separation point of the airfoil cases is further investigated in Fig. 8b. Note that the starting location of actuation is at $X_0 = 0.1$, which is in the vicinity of the leading edge. Keeping the amplitude constant at $a^* = 0.001$ but increasing the angle of attack to 20 deg, the \bar{C}_p plots at $f^* = 8$ and $f^* = 10$ show a significant peak difference from the unactuated case; whereas at $f^* =$ 4 and $f^* = 16$, they are similar to the unactuated case (Fig. 7c). The peak of the C_p plots near the leading edge at $f^* = 8-10$ are significantly higher as compared to the unactuated case (Fig. 7c), which coincides with the maximum lift enhancement observed in Fig. 5. The trend observed at poststall (Fig. 7c) is similar to that of stall (Fig. 7b).

The separation and reattachment points on the airfoil surface are investigated using the mean skin-friction coefficient C_f plot. The separation and reattachment locations on the suction side of the airfoil are defined as where C_f becomes negative and positive, respectively. The flow separation reduces either by pushing the separation downstream or by the reattachment of the separated flow downstream. On the suction side of the unactuated case, the flow separates near the leading edge at X/L = 0.04 and remains separated without flow reattachment. Applying a low-amplitude ($a^* = 0.00006$) wave at stall, the C_f profile remains similar for all the tested nondimensional frequencies, as shown in Fig. 8a. However, the \bar{C}_f profile varies significantly for the higher-amplitude case at stall (Fig. 8b) and poststall (Fig. 8c). Applying a backward-traveling wave actuation of $f^* =$ 4 and $a^* = 0.001$, the flow separation point remains the same at X/L = 0.04, with the skin-friction coefficient profile almost identical to the unactuated case, as shown in Figs. 8b and 8c. Increasing the frequency to $f^* = 8$ and $f^* = 12$ at stall (AOA = 15 deg), the separation point is pushed downstream to X/L = 0.08; reattaches downstream at X/L = 0.13 and X/L = 0.12, respectively; and remains attached until the trailing edge (Fig. 8b). At poststall (AOA = 20 deg), the flow was found to remain attached until the trailing edge, with no separation point near the leading edge with the frequencies of $f^* = 8$ and $f^* = 10$ (Fig. 8c). At these frequencies, the highest lift enhancement, drag reduction, and suction pressure coefficient were observed in Figs. 5,6, and 8, respectively. Increasing the frequency further to $f^* = 16$, the flow separates near the leading edge at X/L = 0.04 with no reattachment, similar to the unactuated and $f^* = 4$ cases (Figs. 8b and 8c). Downstream of the reattachment point, the pressure recovery and the skin-friction coefficient behave

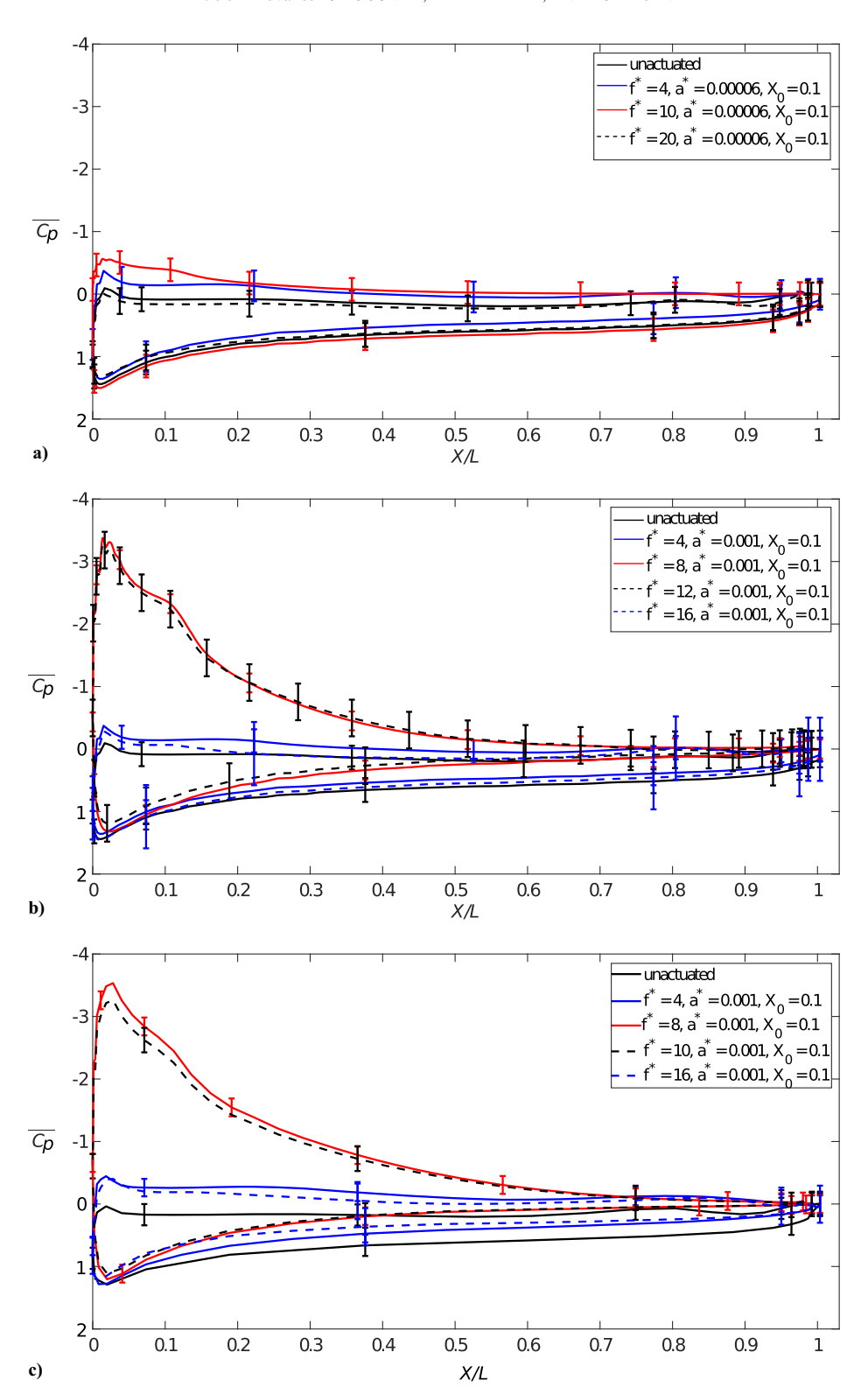


Fig. 7 Effect of frequency on pressure coefficient \bar{C}_p for airfoil with starting location of oscillation of $X_0 = 0.1$: a) AOA = 15 deg and amplitude $a^* = 0.00006$, b) AOA = 15 deg and amplitude $a^* = 0.001$, and c) AOA = 20 deg and amplitude $a^* = 0.001$.

similarly for both unactuated and actuated cases (Fig. 8). Near the trailing edge (x/L > 0.9), a positive $\bar{C_f}$ ($\bar{C_f} > 0$) value occurs for both the unactuated and actuated cases (Fig. 8). However, this high positive value occurs due to the trailing-edge vortex in the flow [33].

B. Effect of Amplitude

The effect of amplitude on the mean C_L and C_D is investigated by testing the following actuation amplitudes: $a^* = 0.0005$, 0.001, 0.002, and 0.004. The low-amplitude actuation ($a^* = 0.00006$) is

not plotted because it is ineffective in improving the aerodynamic performance (lift and drag), as discussed in Sec. III.A. The non-dimensional frequency and starting location of oscillation are kept constant at $f^{\ast}=8$ and $X_{0}=0.1$, respectively, which showed the maximum performance (Figs. 5 and 6) in Sec. III.A. The effects of the amplitude on the mean C_{L} and C_{D} are presented in Figs. 9 and 10, respectively. It can be observed in Fig. 9 that for an actuation with the amplitude of $a^{\ast}=0.0005,\ C_{L}$ and C_{D} remain statistically similar (p>0.05) to the unactuated case. Increasing the amplitude to

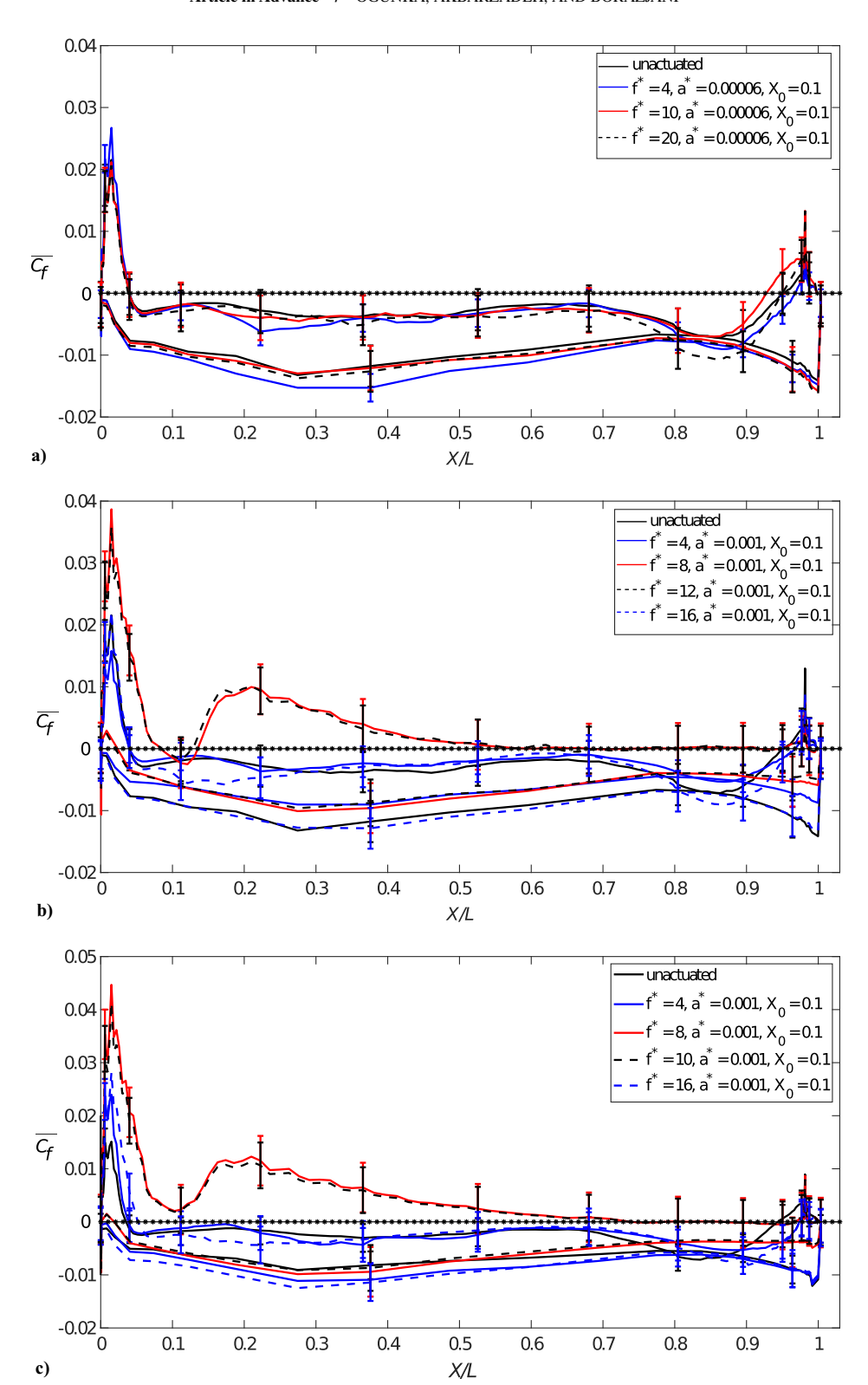


Fig. 8 Effect of frequency on skin-friction coefficient $\vec{C_f}$ for airfoil with starting location of oscillation of $X_0 = 0.1$: a) AOA = 15 deg and amplitude $a^* = 0.00006$, b) AOA = 15 deg and amplitude $a^* = 0.001$, and c) AOA = 20 deg and amplitude $a^* = 0.001$.

 $a^*=0.001$, C_L significantly increases by 32% (p<0.05) and C_D reduces significantly by 68% (p<0.05) as compared to the unactuated case. Increasing the amplitude further to $a^*=0.002$, C_L and C_D remain statistically similar (p>0.05) to $a^*=0.001$ (case 8). Nevertheless, C_L and C_D are significantly (p<0.05) higher and lower, respectively, as compared to the unactuated case. Increasing the amplitude further to $a^*=0.004$, C_L insignificantly decreases by 3% (p>0.05) as compared to $a^*=0.001$ (case 8) but is still significantly higher than the unactuated case by 21% (p<0.05).

Similarly, C_D increases insignificantly by about 11% (p > 0.05) as compared to the $a^* = 0.001$ case, whereas it is still significantly less than (p < 0.05) the unactuated case.

The observed trends of variation of C_L and C_D with actuation amplitude can be explained by the distribution of the mean \bar{C}_p and \bar{C}_f along the airfoil chord, which are depicted in Figs. 11 and 12, respectively. The error bars represent the standard deviations of the mean C_p and C_f for the time cycle duration. Whereas a low-amplitude traveling wave $(a^* = 0.0005)$ does not change the

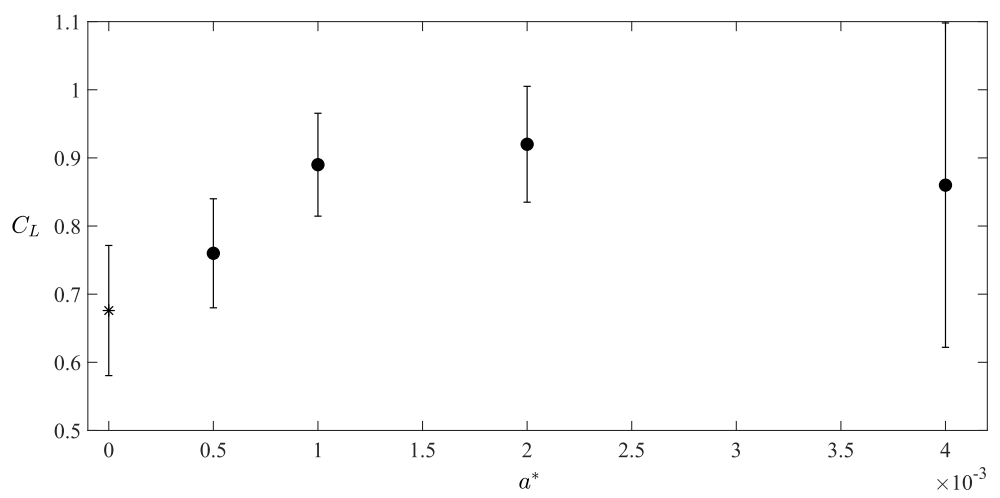


Fig. 9 Effect of amplitude on lift coefficient C_L for airfoil at AOA = 15 deg with frequency of $f^* = 8$ and starting location of oscillation of $X_0 = 0.1$. Unactuated case is represented by an asterisk.

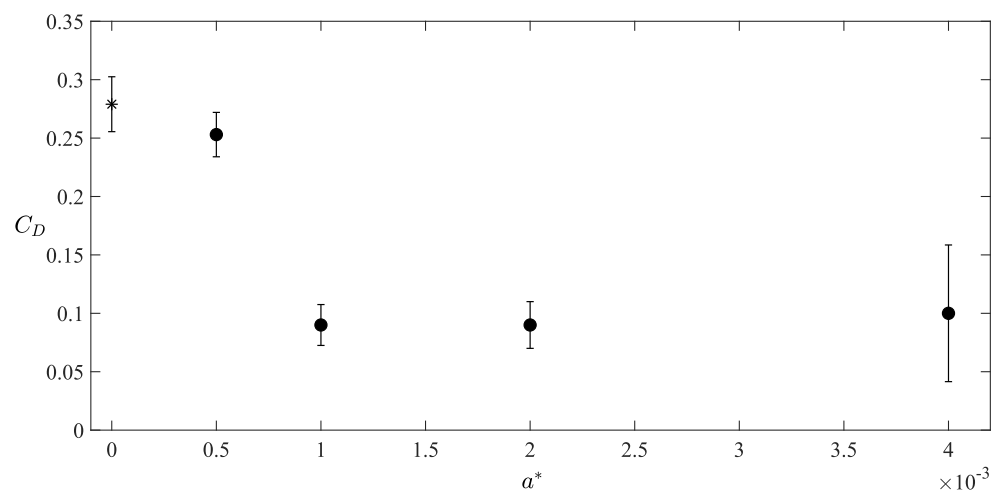


Fig. 10 Effect of amplitude on drag coefficient C_D for airfoil at AOA = 15 deg with frequency of $f^* = 8$ and starting location of oscillation of $X_0 = 0.1$. Unactuated case is represented by and asterisk.

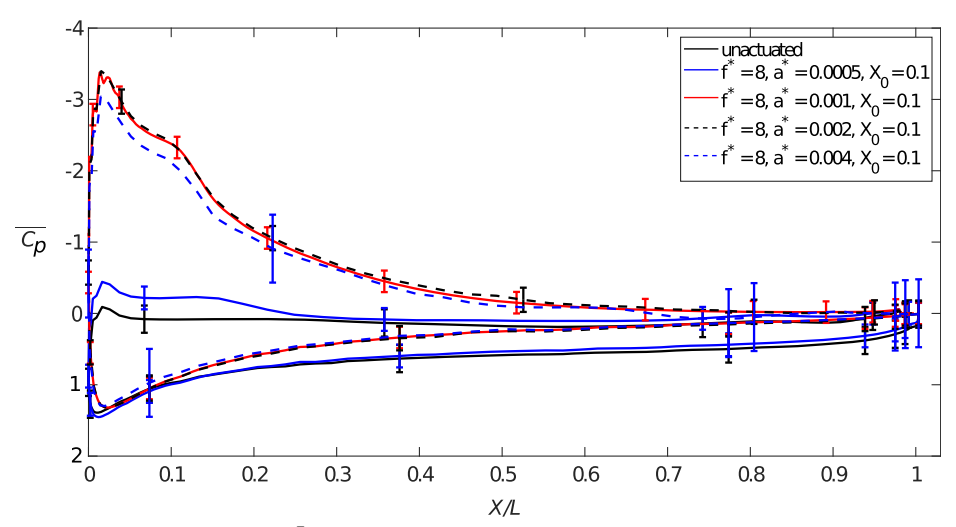


Fig. 11 Effect of amplitude on pressure coefficient \bar{C}_p for airfoil at AOA = 15 deg with frequency $f^* = 8$ and starting location of oscillation of $X_0 = 0.1$.

 $\bar{C_p}$ profile, increasing the amplitudes to $a^*=0.001$ and $a^*=0.002$ modifies $\bar{C_p}$; i.e., the pressure coefficient reduces significantly near the leading edge, with a peak $\bar{C_p}$ at X/L=0.014. At these amplitudes, we observed the highest lift enhancement, as shown in Fig. 9.

Pressure recovery occurs from the peak at X/L = 0.014 toward the trailing edge. Further increasing the amplitude to $a^* = 0.004$, the pressure coefficient reduces near the leading edge as compared to the unactuated case but increases slightly relative to $a^* = 0.001$ and

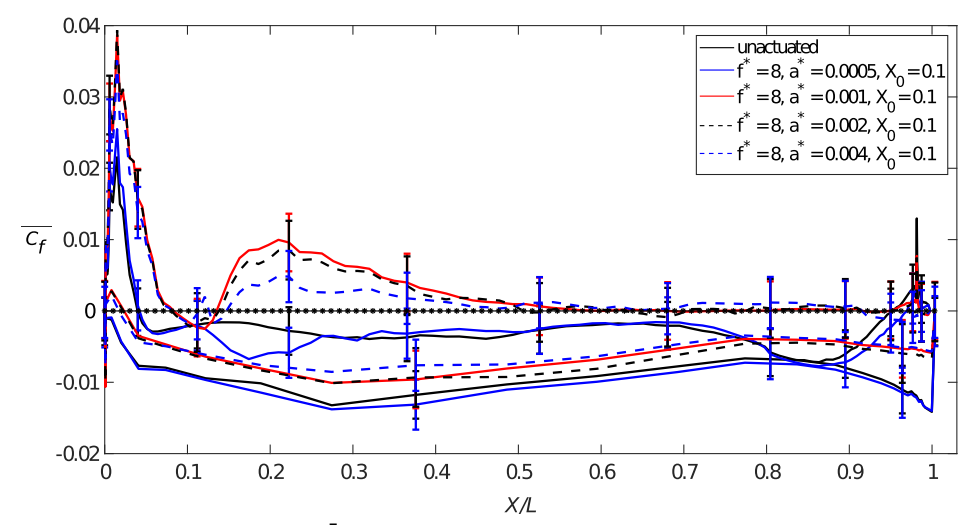


Fig. 12 Effect of amplitude on skin-friction coefficient $\bar{C_f}$ for airfoil at AOA = 15 deg with frequency $f^* = 8$ and starting location of oscillation of $X_0 = 0.1$.

0.002 with its peak at X/L = 0.014 and pressure recovery occurring downstream toward the trailing edge.

The flow separation is investigated by plotting \bar{C}_f (Fig. 12). On the suction (upper) side of the unactuated case, the flow separates near the leading edge at X/L=0.04 and remains separated without flow reattachment. Whereas a low-amplitude actuation ($a^*=0.0005$) does not change the flow separation, actuations with $a^*=0.001$ and $a^*=0.002$ reduce the flow separation by moving the separation point toward downstream and reattaching the flow. At these amplitudes, the separation occurs at X/L=0.08 and reattaches downstream at X/L=0.13 (Fig. 12). The flow remains attached downstream toward the trailing edge. Further increasing the frequency to $a^*=0.004$, the flow separates near the leading edge at X/L=0.08 but reattaches at X/L=0.14 and remains reattached downstream toward the trailing edge.

C. Effect of Starting Location of Oscillation

The effect of the starting location of oscillation on the mean C_L and C_D is investigated by testing the following locations: $X_0 = 0.0, 0.1$, and 0.2. The nondimensional frequency and amplitude are kept constant at $f^* = 8$ and $a^* = 0.001$, respectively. At these values, the maximum lift enhancement and drag reduction were observed as shown in Secs. III.A and III.B. The effect of the starting location of oscillation on the mean C_L and C_D is presented in Figs. 13 and 14, respectively. Figures 13 and 14 show that C_L significantly increases and C_D significantly decreases (p < 0.05) when positioned at $X_0 = 0.05$

0.0 and $X_0=0.1$, but they are not significantly different at $X_0=0.2(p>0.05)$. At $X_0=0.0$, C_L significantly increases and C_D significantly reduces by 33 and 68%, respectively, as compared to the unactuated case (p<0.05). Increasing the starting location of oscillation to $X_0=0.1$, both C_L and C_D remain statistically similar (p>0.05) to the previous case (case 7) at $X_0=0.0$ but are significantly higher and lower, respectively, as compared to the unactuated case (p<0.05). However, increasing the starting location of oscillation to $X_0=0.2$, C_L and C_D become statistically similar (p>0.05) to the unactuated case.

These trends in C_L and C_D are investigated by inspecting the pressure and skin-friction coefficient profiles in Figs. 15 and 16, respectively. On the suction side of the unactuated case, \bar{C}_p decreases near the leading edge, peaking at X/L=0.02. Then, it increases and keeps a flat profile within the range of 0.07 < X/L < 0.8. Applying a backward-traveling wave actuation at $X_0=0.0$ and $X_0=0.1$, where the highest lift was observed (Fig. 13), there is a significant decrease in the pressure coefficient near the leading edge at X/L=0.014. After which, pressure recovery is observed downstream toward the trailing edge. Increasing the starting location of oscillation to $X_0=0.2$, the pressure coefficient significantly reduces near the leading edge as compared to $X_0=0.0$ and $X_0=0.1$, with the peak \bar{C}_p at X/L=0.014. Pressure recovery occurs from the peak at X/L=0.014 toward the trailing edge.

The flow separation is investigated by plotting \tilde{C}_f (Fig. 16). On the suction (upper) side of the unactuated case, the flow separates near

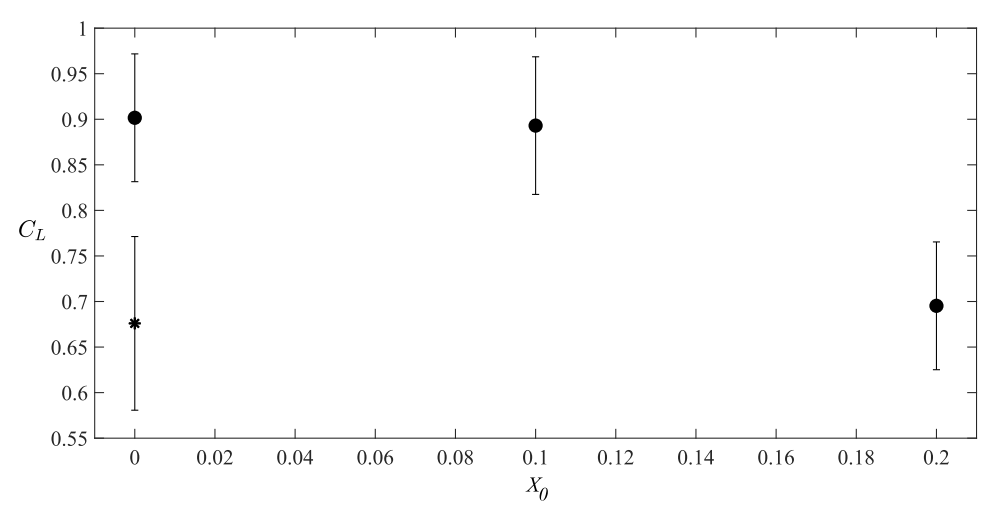


Fig. 13 Effect of starting location of oscillation on lift coefficient C_L for airfoil at AOA = 15 deg with amplitude $a^* = 0.001$ and frequency $f^* = 8$. Unactuated case is represented by an asterisk.

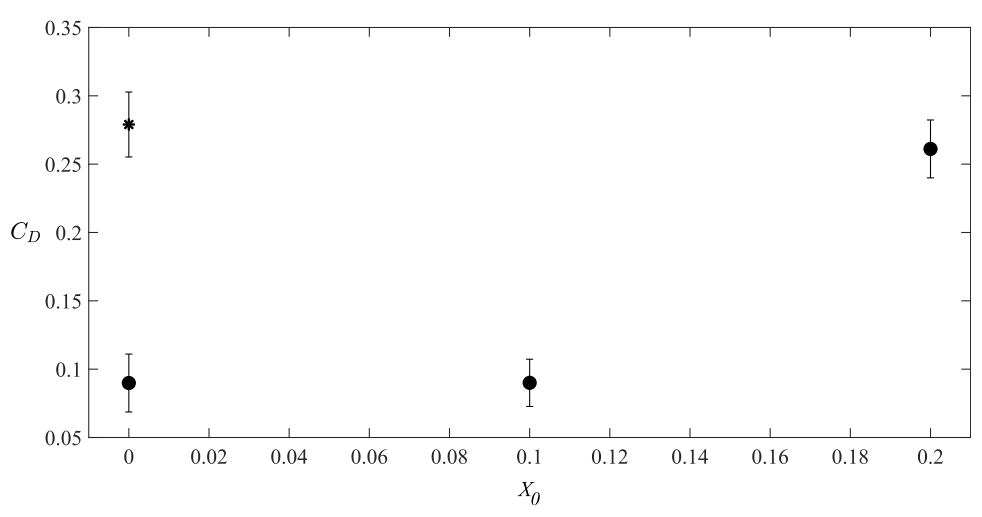


Fig. 14 Effect of starting location of oscillation on drag coefficient C_D for airfoil at AOA = 15 deg with amplitude $a^* = 0.001$ and frequency $f^* = 8$. Unactuated case is represented by an asterisk.

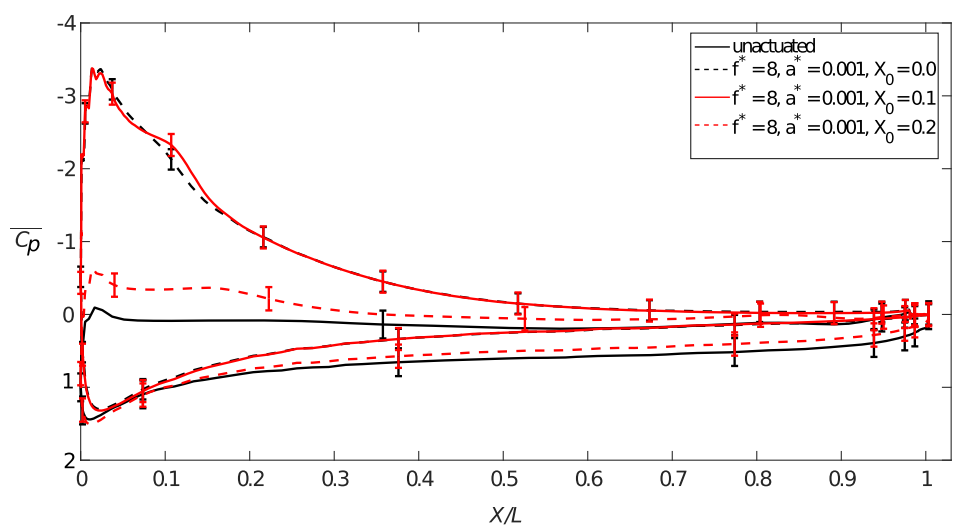


Fig. 15 Effect of starting location of oscillation on pressure coefficient \bar{C}_p for airfoil at AOA = 15 deg with amplitude $a^* = 0.001$ and frequency $f^* = 8$.

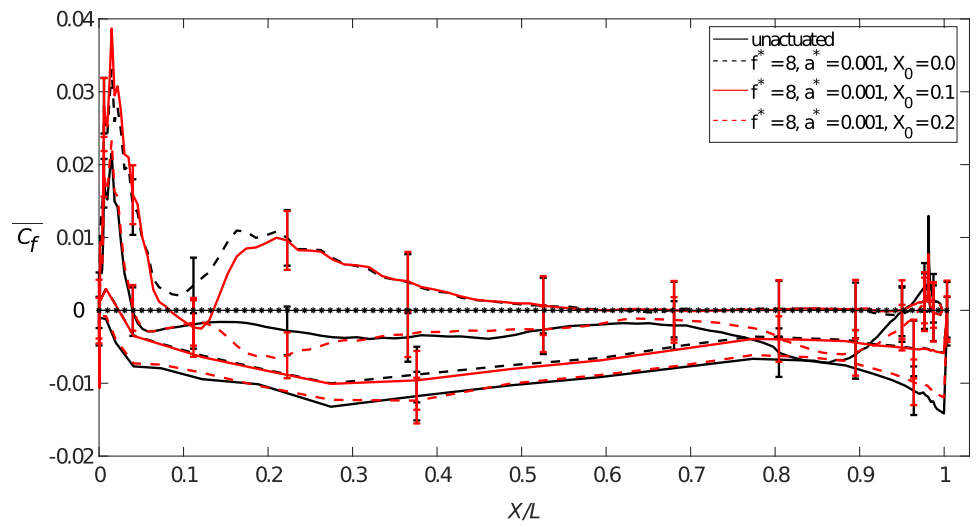


Fig. 16 Effect of starting location of oscillation on skin-friction coefficient $\bar{C_f}$ for airfoil at AOA = 15 deg with amplitude $a^* = 0.001$ and frequency $f^* = 8$.

the leading edge at X/L=0.04 and remains separated without flow reattachment. Applying a backward-traveling wave actuation at $X_0=0.0$, the flow does not separate but remains attached downstream from the leading edge to the trailing edge. Increasing the

starting location of oscillation to $X_0 = 0.1$, the separation point occurs at X/L = 0.08 and reattaches downstream at X/L = 0.13. The flow remains attached downstream toward the trailing edge. The reattachment of the flow near the leading edge occurs during the

pressure recovery of the suction (upper) side of the airfoil, as shown in Fig. 15. Increasing the starting location of oscillation to $X_0=0.2$, the flow separates near the leading edge at X/L=0.04, with no reattachment. Based on the preceding information, when the flow does not separate ($X_0=0.0$) or reattach ($X_0=0.1$) due to the actuation, C_L increases and C_D decreases.

D. Flowfield

The effect of oscillations for all the cases presented in Table 1 can be observed by the instantaneous flowfield (instantaneous contours of the out-of-plane vorticity) in Figs. 17 and 18 at four different phases of the cycle $(0, 1/4f^*, 1/2f^*, \text{ and } 3/4f^* \text{ in columns } 1 \text{ to } 4 \text{ of Figs. } 17 \text{ and } 1/4f^*$ 18, respectively). Figures 17 and 18 show the contours of the spanwise vorticity at stall (AOA = 15 deg) and poststall (AOA = 20 deg), respectively. For unactuated cases 1 (AOA = 15 deg) and 15 (AOA = 20 deg), the flow is highly separated; i.e., the shear layer separates from the leading edge of the airfoil and a large recirculation (trailing-edge vortex) is generated near the trailing edge. Although a traveling wave with a low amplitude of $a^* \le 0.0005$ (cases 2–5) was prescribed on the airfoil at stall (AOA = 15 deg), the flow separation was not suppressed (Figs. 17b-17e). However, by increasing the amplitude of the oscillation to $a^* = 0.001-0.004$, keeping the frequency range of 8 to 12, and starting the location of the oscillation range from $X_0 = 0.0$ to $X_0 = 0.1$ in cases 7, 8, 10, 12, and 13, the shear layer is attached on the leading edge of the airfoil and the large recirculation zone is eliminated (Fig. 17). In fact, reducing the size of the actuated surface from 100 to 10% (case 14b) did not significantly alter the flow reattachment. The flow remained reattached to the upper surface with the corresponding reduction in the large recirculation zone near the trailing edge, as shown in Fig. 17o. This flow reattachment is also observed when the angle of attack is increased to AOA = 20 deg, with the amplitude set to $a^* = 0.001$, the starting location of oscillation set to $X_0 = 0.1$, and the frequency range of $f^* = 8-10$, as shown in cases 17 and 18 (Figs. 18b and 18c). Nevertheless, by increasing the frequency in case 11 (AOA = 15 deg) and case 19 (AOA = 20 deg) to $f^* = 16$ or decreasing the frequency in case 6 (AOA = 15 deg) and case 16 (AOA = 20 deg) to $f^* = 4$, the shear layer separation and trailing-edge vortex increase. Flow separation is also observed when increasing the starting location of oscillation from $X_0 = 0.1$ (case 8) to $X_0 = 0.2$ (case 9) at AOA = 15 deg (Fig. 17i). Lastly, the standing wave actuation (case 14) at AOA = 15 deg suppresses stall and reduces the flow separation, as shown in Fig. 17n.

The three-dimensional instantaneous vortical structures visualized by means of the isosurface of the Q criterion [60] for the unactuated case (case 1) and the backward-traveling wave actuated airfoil with $f^* = 8$, $a^* = 0.001$, and $X_0 = 0.1$ (case 8) at AOA = 15 deg, as well as the unactuated case (case 15) and the actuated case with $f^* = 8$, $a^* = 0.001$, and $X_0 = 0.1$ (case 17) at AOA = 20 deg are shown in Fig. 19. From Figs. 19a and 19c, the flow starts to separate near the leading edge of the airfoil and fails to reattach to the airfoil surface. The separation is characterized by a large recirculation zone occurring on the suction side of the airfoil. The periodic streamwise vortices move downstream from the leading edge. Large vortex sheddings are formed behind the trailing edge of the airfoil due to the interaction between the structures separated from the turbulent shear layer and the incoming flow along the pressure side of the airfoil. In Figs. 19b and 19d, the airfoil undergoes a backwardtraveling wave actuation of $f^* = 8$, with $a^* = 0.001$ at $X_0 = 0.1$ from the leading edge on the suction side of the airfoil. As the flow propagates downstream, the large vortical structures break down; and they enhance the mixing of the high-momentum separated shear layer with the low-momentum flow near the suction side of the airfoil [6]. The flow separation near the leading edge of the airfoil is reduced significantly. Then, flow reattachment occurs immediately near the leading edge of the airfoil, with the fully turbulent flow moving downstream to the trailing edge.

IV. Discussion

Previous works [33,34,40,41,61] on flow control via traveling wave actuation on airfoils have shown that backward-traveling waves

can suppress stall and reduce flow separation. As mentioned previously, traveling waves influence the flow separation by transfer of momentum by triggering flow instabilities (indirect momentum transfer) and direct injection of streamwise momentum. The relative importance of these mechanisms for traveling waves can be best understood from the effect of the wave parameters on the flow separation. In this section, the importance of these mechanisms will be discussed based on the trends observed for the different wave parameters, which were reported in Sec. III. In addition, the findings will be compared against the previous work; and the performance of the traveling waves at different angles of attack will be discussed.

A. Mechanisms of Flow Control

The thrust force generated by traveling waves is of order $\mathcal{O}\{a^{*2}[f^*-(1/\lambda^*)]^2\}$ [34], which is derived from Lighthill's elongated body theory [35]. Although EBT assumes inviscid flow, it can serve as a good scaling for the thrust force of traveling wave surfaces because it is mainly based on the added mass argument [34,35], which is still valid for viscous flows. Therefore, if injecting streamwise momentum is the dominant mechanism, then increasing the amplitude a^* or frequency f^* should decrease the separation. If the triggering of instabilities is dominant, then separation may not decrease if the frequency and amplitude increase. Furthermore, the location of excitation X_0 might alter the growth of instabilities in the flow.

Comparing the flowfields (Figs. 17 and 18) of the unactuated (cases 1 and 15) with the traveling wave actuated cases when $f^* = 8-12$, $a^* = 0.001-0.004$, and $X_0 = 0.0-0.1$ (cases $7,\,8,\,10,\,12^*,\,13,\,17,$ and 18), it is noticeable that there is a reduction in the flow separation. This reduction in the flow separation led to a significant improvement in the aerodynamic performance (lift and drag) of the airfoil (Figs. 5 and 6). However, insignificant differences were observed in the flow separation, lift, and drag as compared to the unactuated case when the frequencies of the traveling wave were $f^* = 4$ and $f^* = 16$. This indicates that there is a range of frequencies at which the traveling waves can reattach the flow. This range is similar to the range of dominant frequencies in leading-edge vortex shedding of the unactuated case (Fig. 4). A range of frequencies for effective flow control has also been observed for other periodic excitations [62-65] for which the main mechanism is triggering flow instabilities [6,16]. Note that increasing the frequency increases the wave speed C^* because the wave speed is dependent on the frequency and wavelength ($C^* = \lambda^* f^*$). Because the wavelength is kept constant in this study, the increase in the frequency causes a corresponding increase in the wave speed. Hence, traveling waves can reattach the flow for a range of wave speeds. Note that the flow separation (compared to the unactuated case) does not reduce when the wave speed is increased above this range. This suggests that the dominant mechanism by which traveling waves reduce flow separation is the indirect momentum transfer via the triggering of flow instabilities.

Although traveling waves with $a^* \le 0.0005$ have similar flow behavior with the unactuated case, increasing the wave amplitude to $0.001 \le a^* \le 0.004$ sees a significant improvement in the lift enhancement and drag reduction. In Fig. 17, it can be seen that the flow separation reduced significantly as compared to the unactuated case. As the wave amplitude was increased from $a^* = 0.001$ to $a^* = 0.004$, there was little variation in the mean lift and drag. This suggests that the wave amplitude, and consequently the $O(a^{*2})$ thrust, generated by traveling waves is not correlated to the lift enhancement and drag reduction. However, the standard deviation of the coefficients of lift and drag at $a^* = 0.004$ increased substantially as compared to $a^* = 0.001-0.002$. This indicates that the data of the lift and drag at $a^* = 0.004$ are less concentrated around the mean value and have a higher variance (spread) of values as compared to those of $a^* = 0.001-0.002$. Therefore, this suggests that the range of the wave amplitude of $0.001 \le a^* \le 0.002$ is more reliable for optimal flow control via traveling waves.

Actuators located near the leading edge can affect the separation point and boundary layer on the suction side of the airfoil [66]. The separation point on the unactuated airfoil was X/L = 0.04, as shown

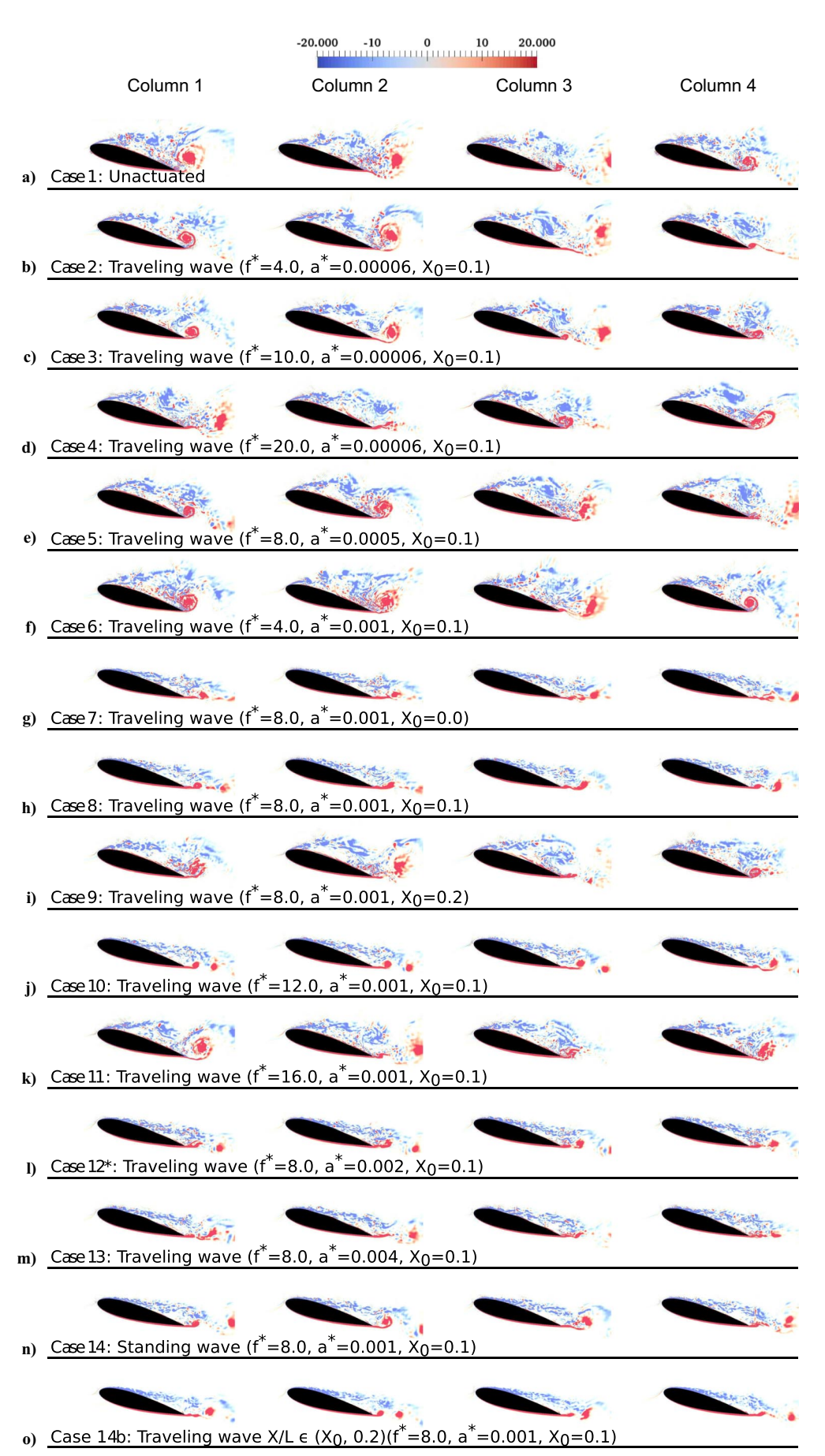


Fig. 17 Contours of instantaneous spanwise vorticity at AOA = 15 deg.

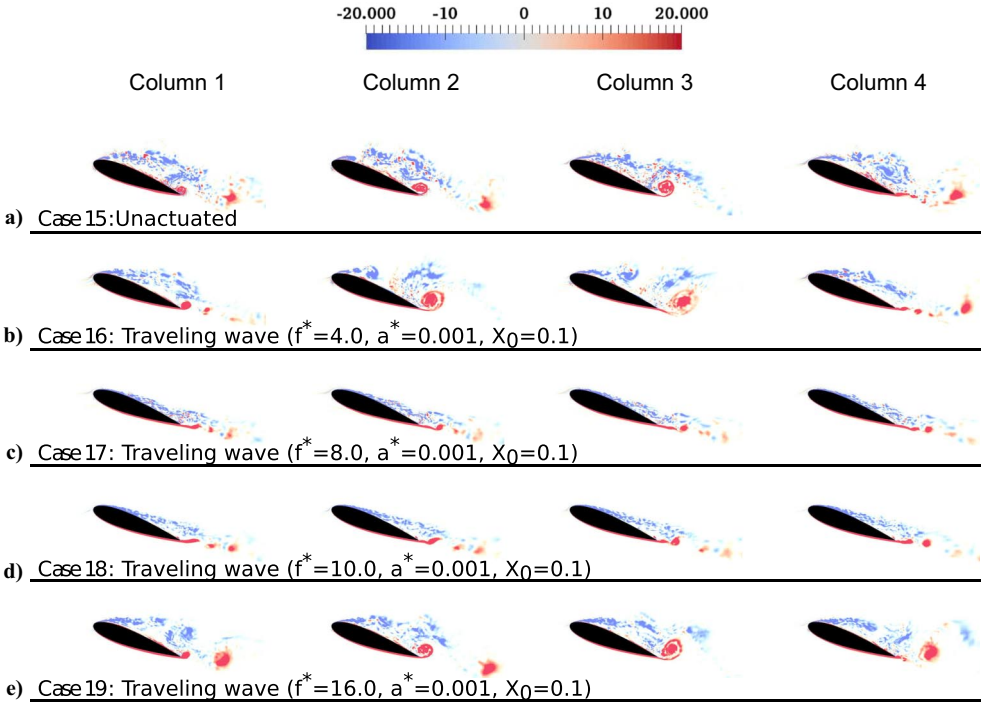


Fig. 18 Contours of the instantaneous spanwise vorticity at AOA = 20 deg.

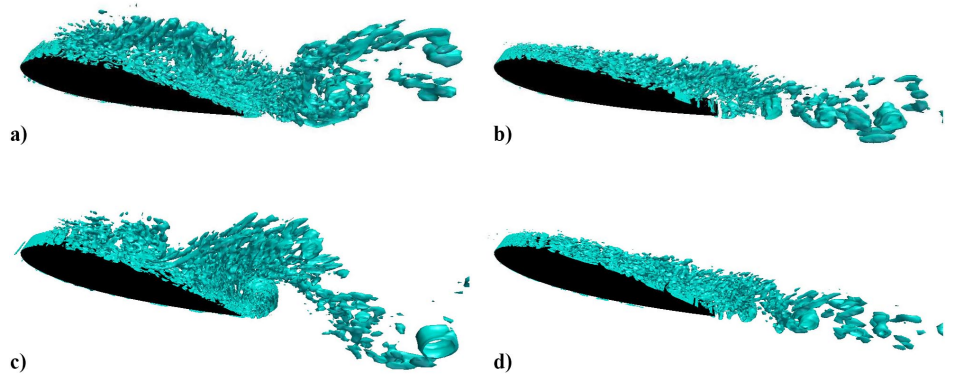


Fig. 19 Three-dimensional vortical structures visualized by isosurface of Q criterion (Q = 20) of NACA0018 airfoil: a) unactuated case and b) actuated case with $f^* = 8$ and $a^* = 0.001$ at AOA = 15 deg; and c) unactuated case and d) actuated case with $f^* = 8$ and $a^* = 0.001$ at AOA = 20 deg.

in Fig. 16. The traveling wave oscillations (with favorable frequency and amplitude) excited near the leading edge (around 10% of the chord length L) significantly suppressed stall, increased the lift, and decreased the drag as shown in Figs. 13 and 14, respectively. The flow separation significantly reduced when the traveling wave actuation was located at $X_0=0.0$ –0.1. However, increasing the starting location of oscillations to $X_0=0.2$ had an insignificant effect on the unactuated airfoil, as shown in Figs. 13 and 14. The reduced effect of the location of oscillation at $X_0=0.2$ on the lift and drag, compared to $X_0=0.0$ and $X_0=0.1$, is due to the unactuated separation point being upstream of $X_0=0.2$, as shown in Fig. 16. This suggests that flow control via traveling waves is dependent on the starting location of oscillation, and it is most effective when the actuation (with the optimal frequency and amplitude) is located near the point of flow separation on the suction side of the airfoil.

Based on the preceding information, it was demonstrated in this study that traveling waves can effectively reduce flow separation. The flow separation was shown to be significantly influenced by the frequency, amplitude, and location of the oscillation. The results show that flow separation is greatly decreased within a frequency range ($f^* = 8$ –12) corresponding to the leading-edge vortex shedding frequency range. Furthermore, ranges of amplitudes ($a^* = 0.001$ –0.002) and oscillation locations ($X_0 = 0.0$ –0.1) were shown to significantly minimize the flow separation. Because flow separation does not reduce

monotonically with frequency and amplitude, and it depends on the oscillation location, the main mechanism is the indirect injection of momentum (triggering instabilities). Identifying which inherent instabilities are triggered by the traveling waves requires a detailed stability analysis, which is beyond the scope of this work.

The main mechanism by which standing waves reduce flow separation is also indirect injection of momentum [6,64,67]. In fact, standing wave actuation suppressed stall and reduced the flow separation, as shown in Fig. 17n. The standing wave significantly increased the lift enhancement and drag reduction as compared to the unactuated case but was less effective as compared to the traveling wave (Table 1). Compared to the traveling wave actuation (case 8) with the same frequency, amplitude, and starting location of oscillation, the standing wave actuation case (case 14) had an 8% significantly lower C_L value (p < 0.05) and an 18% significantly higher C_D value (p < 0.05), as presented in Table 1. Note that the size of the actuated surface was also constant; i.e., the wave oscillation propagated from $X/L = X_0$ to X/L = 0.9. This is probably because traveling waves also directly inject streamwise momentum into the flow [33]. This indicates that if the instabilities are triggered, traveling wave actuators perform better than standing wave actuators because they can use both indirectly injecting momentum via triggering the flow instabilities and directly injecting streamwise momentum into the boundary layer. In fact, it was observed that the traveling

wave actuation (case 14b), with the size of the actuated surface reduced ($X/L \in 0.1, 0.2$), had an 8% significantly higher C_L value (p < 0.05) and an 18% significantly lower C_D value (p < 0.05) (Table 1) as compared to the standing wave actuation but was statistically similar to the traveling wave actuation case with the larger actuated surface (case 8). This provides further evidence that the major mechanism of flow reattachment for traveling waves is the indirect injection of momentum via triggering instabilities.

More analysis on the leading-edge vortex shedding frequency of the unactuated and actuated cases was performed for a quantitative discussion. Figures 20a and 20b show the power spectrum density of the streamwise velocity for the actuated cases with reduced frequency (Fig. 20a) $f^* = 8.0$ (case 8) and (Fig. 20b) $f^* = 16.0$ (case 11). Similar to the unactuated case (case 1) shown in Fig. 4, the spectrum is computed via the fast Fourier transform for a total nondimensional time of $t^* = 220$ at the same location near the leading edge. As shown in the Results section (Sec. III), Fig. 4 shows that the power spectrum density peak of the unactuated airfoil is within the range of $f^* = 6-10$. In fact, it has been observed in the literature that the power spectrum density peak of the vortex shedding frequency of the unactuated airfoil corresponds to the frequency of the most unstable linear mode disturbance [68–70]. For the actuated case with $f^* = 8$ (case 8) presented in Fig. 20a, the highest peak of the leading-edge vortex shedding frequency is observed at $f^* = 8$, which corresponds to the frequency of the traveling wave oscillation of $f^* = 8$. Spectra peaks of less magnitude are also observed at $f^* = 2, 6, 10,$ and 12. The flow separation is observed to be reduced significantly such that flow reattachment occurred (Fig. 17h). This is probably because the

 $f^* = 8$ actuated case excited the Kelvin–Helmholtz instability, which amplified the leading-edge vortex shedding frequency in the shear layer [69]. The amplification of the vortex shedding frequency led to the promotion of transition of the shear layer to turbulence [68,70-72]. This indicates that the growth of the power spectra density is significant near the shedding frequency ($f^* = 6-10$) of the unactuated case. The frequency of the traveling wave, $f^* = 8$, is within the range of the shedding frequency of the leading-edge vortex. Sato et al. [70] observed that the vortex shedding frequency of the separated shear layer is closely related to the peak frequency of the natural unstable mode of the shear layer using linear stability analysis. Hence, this indicates that if the frequency of the actuation is near the leading-edge vortex shedding frequency of the unactuated case, transition of the shear layer to turbulence is promoted, thereby resulting in flow reattachment and significant improvements in the aerodynamic performance (lift and drag). For the actuated case with $f^* = 16$ shown in Fig. 20b, the highest peak of the power spectra density is observed at $f^* = 16$. The peak corresponds to the frequency of the actuation. A smaller distinct spectra peak is observed at the subharmonic of $f^* = 8$. However, the excitation of the natural unstable mode does not significantly suppress the flow separation, as shown in Fig. 17k. Flow reattachment is not observed, and there are insignificant changes in the aerodynamic performance (lift and drag).

Sato et al. [70] observed that for flows within the Reynolds number range of $50,000 \le Re \le 200,000$, an important mechanism for flow reattachment was the transition of the laminar boundary layer to turbulence. This suggests that effective flow control methods for flows of $10^3 \le Re \le 10^6$ may not work for flows with higher

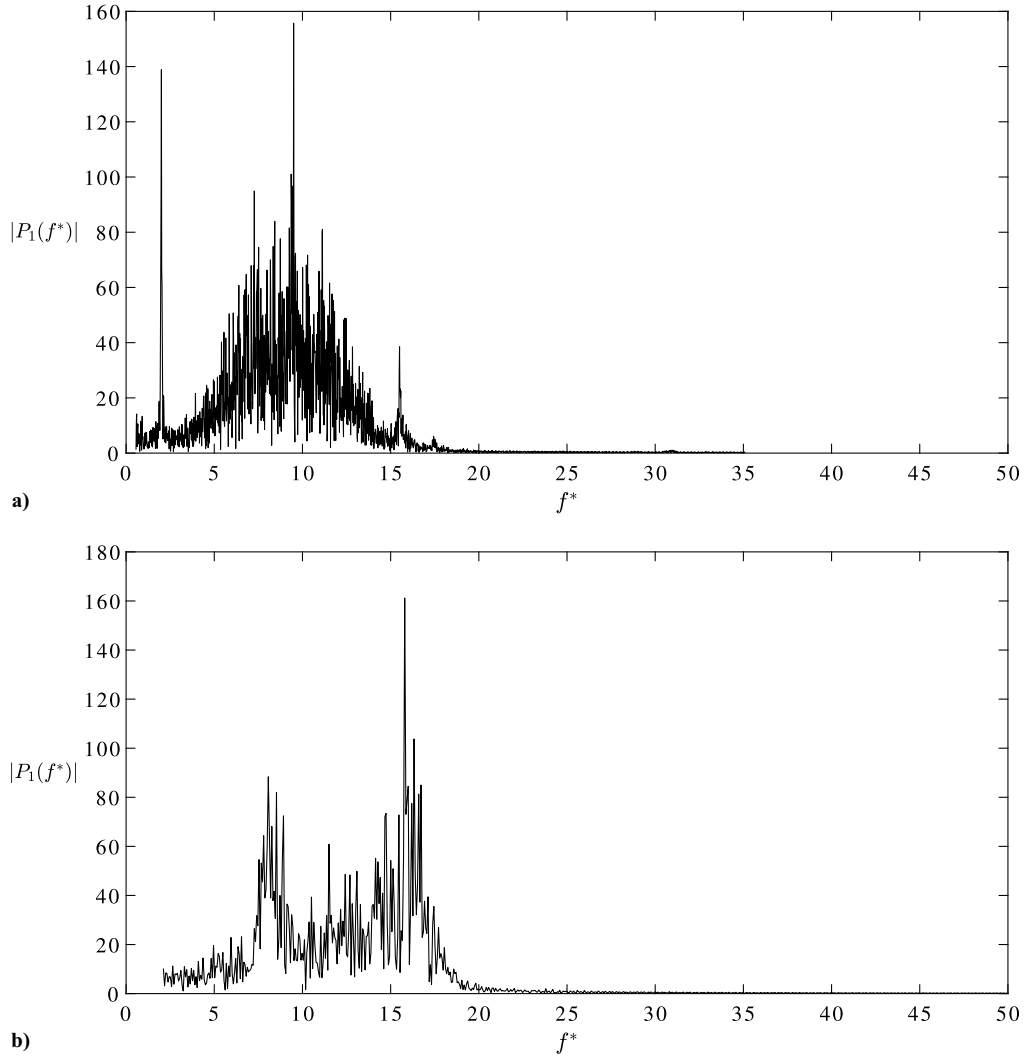


Fig. 20 Power spectrum density plot of velocity P_1 in frequency domain for actuated airfoil with amplitude of $a^* = 0.001$, starting location of oscillation of $X_0 = 0.1$, and reduced frequencies of a) $f^* = 8$ and b) $f^* = 16$ at AOA = 15 deg near leading edge.

Reynolds numbers ($Re \ge 10^6$) where the boundary layer is already turbulent. Hence, a different strategy for flow control methods would be needed for separated turbulent flows ($Re \ge 10^6$) [70–73]. Understanding the effect of Reynolds numbers on flow separation control via traveling waves at the stall and poststall angles of attack is an interesting topic for future studies.

B. Comparison with Previous Work

As discussed in the previous subsection (Sec. IV.A), the dominant mechanism for traveling waves and periodic excitations is the same. A similar frequency bound has been observed for periodic excitations. Lei et al. [62], in their numerical investigations of the effect of sinusoidal oscillations on an airfoil, observed significant lift enhancement and drag reduction when the nondimensional frequency was equivalent to the vortex shedding frequency. However, significant reductions in the lift enhancement and drag reduction were observed when the nondimensional frequency was greater than double the shedding frequency. The size of the flow separation increased as the frequency increased above the shedding frequency, having a similar size to the unactuated airfoil. Thompson and Goza [74] numerically studied the effect of traveling waves at Re = 1000. They observed that the wave speed and wave number can influence the lift and drag of the airfoil. Note that wave number is the reciprocal (inverse) of the wavelength. They observed that increasing the wave speed with a corresponding increase in frequency (at a constant wave number) does not monotonically increase the lift enhancement and drag reduction. In fact, they observed that a range of wave speed with a corresponding range of frequency, which was similar to the range of the shedding frequency, led to a significant lift enhancement and drag reduction. Outside the range of the shedding frequency, negligible changes in the lift and drag were observed. Other flow control via periodic excitations [63,75] also observed a loss in lift and increase in drag when the frequency was increased above the vortex shedding frequency. This would suggest that flow control that incorporates the mechanism of indirect momentum transfer via has a frequency bound beyond which flow separation might not reduce. This is in stark contrast to flow control via direct injection of streamwise momentum mechanism, e.g., suction and blowing, where the lift enhancement and drag reduction were observed to be independent of the frequency [76]. Our work on traveling waves observed that increasing the amplitude of traveling wave oscillation within the range of $0.001 \le$ $a^* \le 0.004$ reattached the flow and significantly improved the lift enhancement and drag reduction. An insignificant influence was observed when the amplitude was increased from $a^* = 0.001$ to $a^* = 0.004$. Lei et al. [62] performed numerical investigations on sinusoidal wavy oscillations on the airfoil's upper surface at Re =30,000 and AOA = 4 deg. They observed that increasing the amplitude to $a^* = 0.001$ led to an increase in the lift enhancement and drag reduction. In addition, they observed that the flow reattached at $a^* = 0.001$. However, increasing the amplitude toward $a^* =$ 0.005 saw an insignificant reduction in the lift and drag. For periodic excitations (flow reattachment mechanism via triggering flow instabilities), the wave amplitude seemed to be not linearly related to the lift enhancement and drag reduction [63]. Contrary to the mechanism of indirect momentum injection via triggering flow instabilities, the mechanism of direct injection of momentum has been seen to observe a more direct effect due to amplitude. Huang et al. [77] observed that increasing the suction amplitude resulted in a significant linear increase in the lift enhancement and drag reduction. They also observed a reduction in flow separation as the suction amplitude increased [77]; although, the opposite effect was observed for blowing because increasing the blowing amplitude caused an increase in the drag and flow separation [77]. Compared to the flow reattachment mechanism via triggering flow instabilities, the direct injection of momentum seems to observe a linear relationship between the suction amplitude and the improvement in lift enhancement and drag reduction. As mentioned earlier, the location of oscillation has a significant impact on the aerodynamic performance (lift and drag) of traveling wave actuations. We observed that the closer the actuator was to the leading edge ($X_0 = 0.0-0.1$), the better the aerodynamic performance. The flow separation was reduced significantly when the actuator was within the vicinity of the leading edge. The dependence on location has been typically observed in flow control using periodic excitations and vortex generators. Hsiao et al. [21] experimentally investigated the flow control over an airfoil via acoustic excitation vibrations at Re = 300,000 and AOA = 18-22 deg (poststall) and observed the maximum improvement in lift with the actuation located nearest to the leading edge ($X_0 = 0.0125$) than when located further downstream ($X_0 = 0.1325$). Post and Corke [78] experimentally compared the flow control performance of vortex generators and plasma actuators on an airfoil at different locations from the leading edge at Re = 79,000-158,000. They observed that both vortex generators and plasma actuators performed better when located closer to the leading edge. Sato et al. [72,79] also observed significant lift enhancement and drag reduction when the plasma actuator was located upstream of the separation point near the leading edge. Donovan et al. [66] numerically investigated the active flow control over a NACA0012 airfoil at $Re = 8.5 \times 10^6$ via synthetic jets. They observed that the effects of flow control were more significant when the actuator was located closer to the leading edge at $X_0 = 0.015$ than when positioned farther off at $X_0 = 0.14$. Feero et al. [65] experimentally studied the effect of synthetic jet location on flow control over a NACA0025 airfoil at Re = 100,000 and AOA = 12 deg. They observed the largest significant increase in the lift-to-drag ratio when the synthetic jet slot was located upstream of the separation point, near the leading edge. This would imply that the effectiveness of the mechanism of indirect momentum injection via triggering flow instabilities on flow control is highly dependent on the location of the actuator. However, flow control via the mechanism of direct injection of streamwise momentum is independent of the effect of actuator location. Suction and blowing have been observed to influence flow control positively when located either near the leading edge or trailing edge [77,80-87]. Hence, we can deduce that the location of the actuator plays a more significant role in flow control via indirect transfer of momentum by triggering flow instabilities as compared to flow control via direct injection of streamwise momentum mechanism.

C. Stall Delay by Traveling Waves

The preceding results and discussion were based on the stall and poststall angles of attack (AOA = 15-20 deg). Here, we investigate the impact of traveling waves actuation at different angles of attack, including the prestall angles of attack (AOA = 10 deg) [37]. Figures 21a and 21b present the lift and drag coefficients as a function of angle of attack for both the unactuated (baseline) and actuated airfoils. The actuated airfoils are the ones that showed the highest performance (Sec. III.A) with a surface traveling wave actuation of nondimensional frequency of $f^* = 8.0$, an actuation amplitude of $a^* = 0.001$, and the starting location at $X_0 = 0.1$ from the leading edge. The lift coefficient of the unactuated airfoil increases linearly as the angle of attack increases. The peak C_L of the unactuated airfoil is achieved at AOA = 10 deg. Beyond AOA = 10 deg, the lift coefficient decreases significantly as the angle of attack increases toward AOA = 20 deg. As for the drag coefficient, C_D increases slightly as the angle of attack increases (AOA = 0-10 deg). As the angle of attack increases beyond AOA = 10 deg, there is a dramatic increase in the drag coefficient as the angle of attack increases toward AOA = 20 deg. These significant changes in C_L and C_D at AOA =15 deg suggest that the airfoil has experienced the effects of stall. Hence, AOA = 15 deg is the stall angle, and the poststall occurs at AOA \geq 15 deg.

For the actuated airfoil, there is an increase in the lift and a decrease in the drag. At the prestall angle (AOA = 10 deg), the lift coefficient increases by 4% and the drag coefficient reduces by 9% as compared to the unactuated airfoil. As the angle of attack is increased, the effect of the traveling wave flow control becomes more significant. At the stall angle (AOA = 15 deg), C_L significantly increases by 32% (p < 0.05) and the C_D significantly reduces by 68% (p < 0.05) as compared to the unactuated airfoil. At the poststall angle (AOA = 20 deg), the significant percentage increase in C_L is 23%

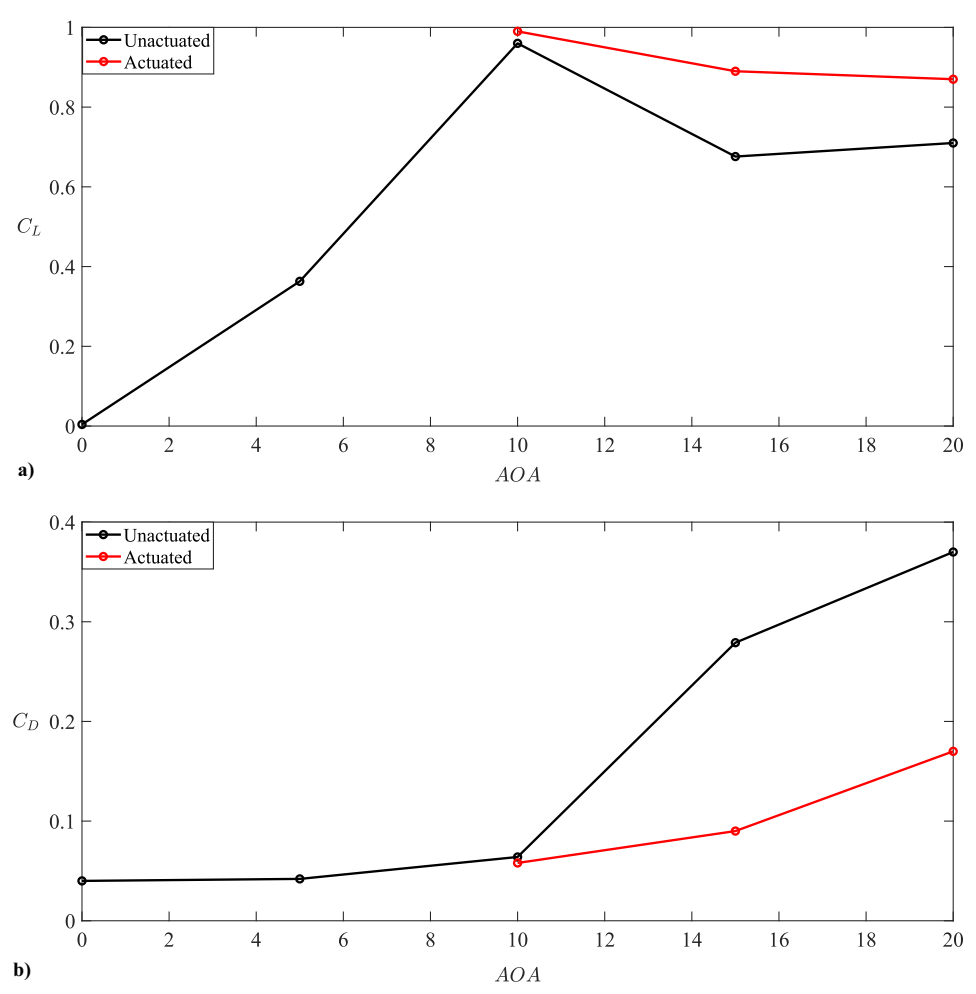


Fig. 21 Representations of a) lift C_L and b) drag C_D curves of baseline (unactuated) and actuated ($f^* = 8.0, a^* = 0.001$) airfoils against angles of attack from 0 to 20 deg.

(p < 0.05), and the significant percentage decrease in C_D is 54% (p < 0.05) as compared to the unactuated airfoil. These results demonstrate that the traveling waves are an effective flow control method at stall and poststall regions.

V. Conclusions

To investigate the mechanisms of flow control by traveling waves, the effects of the nondimensional frequency, amplitude, and starting location of oscillation of traveling waves on the flow and performance of a NACA0018 airfoil at stall (AOA = 15 deg) and poststall (AOA = 20 deg) conditions were investigated numerically by varying f^* from $f^* = 4$ to $f^* = 20$, amplitudes from $a^* = 0.00006$ to $a^* = 0.004$ and by ranging the starting location of oscillation from $a^* = 0.00006$ to $a^* = 0.004$. The flow was visualized, and the aerodynamic performance metrics $(C_L, C_D, \bar{C}_p,$ and $\bar{C}_f)$ were calculated.

Traveling wave actuations affect flow separation by employing two mechanisms: 2) direct injection of momentum in the streamwise direction, and 2) indirect injection of momentum via triggering flow instabilities. The mechanism of indirectly injecting momentum by triggering instabilities and transitioning the boundary layer to turbulence is found to be dominant because frequency has bounds and the starting location needs to be close to where the instabilities can be triggered. At $a^* = 0.001$ and $X_0 = 0.1$ (stall and poststall), the ranges of frequencies for the maximum lift enhancement and drag reduction were $8 \le f^* \le 12$ (stall) and $8 \le f^* \le 10$ (poststall). Stall was suppressed, and flow reattachment occurred. Also, the maximum lift enhancement, drag reduction, and flow separation occurred at the starting location of oscillation ($X_0 \le 0.1$) near the vicinity of the flow separation point. Moreover, the range of the wave amplitude for the

maximum lift enhancement and drag reduction was $a^* \ge 0.001$; but, to reduce the standard deviation of the coefficients, $a^* \le 0.002$. When the instabilities were successfully triggered, the injection of the streamwise momentum of traveling waves improved the performance relative to standing waves. This was because standing waves reduced the flow separation by only indirectly injecting momentum via triggering the flow instabilities. Traveling waves have an extra advantage due to directly increasing the streamwise momentum of the shear layer.

Appendix: Grid Sensitivity and Grid Convergence Analysis

To investigate the grid sensitivity of the airfoil simulations, a grid refinement study on the LESs of a NACA0018 airfoil was performed using three O-grid meshes. The grid refinement study of the grid was performed to ensure the results of the simulations were independent of the grid for both the unactuated and actuated flows. Additionally, convergence analysis results were reported to show the order of accuracy of the numerical scheme. The stall angle of attack of 15 deg and the Reynolds number of Re = 50,000 were selected for the study, and the mean coefficients of the lift C_L and drag C_D were examined for about 40 nondimensional time units ($t^* = tU/L$) for the unactuated flow. For the actuated airfoil, the surface actuation selected was the traveling wave with a reduced frequency of $f^* = 8.0$, an amplitude of $a^* = 0.001$, and a starting location of oscillation of $X_0 = 0.1$. The mean coefficients of the lift C_L and drag C_D were computed by averaging about 10 cycles for the actuated flow. Details about the grid domain and the mean coefficients of the lift and drag of the unactuated and actuated flows are shown in Tables A1 and A2, respectively. A number of points along ξ , η , and

Table A1	Details of the co	omnutational	moch arid	for unactuated flow
rame a r	Details of the C	omomanonai	mesn gria	ior iiliaciliated ilow

Grid	N_{ξ}	N_{η}	N_{ζ}	$\delta \xi_{ m min}^+$	$\delta\eta_{ m min}^+$	$\delta\zeta_{ m min}^+$	$\Delta l_{\xi}^{ ext{min}}$	$\Delta l_{\eta}^{ m min}$	$\Delta l_{\zeta}^{ m min}$	C_L	C_D
1	213	141	13	2.0	1.4	21.7	0.008L	0.0006L	0.008L	0.672	0.274
2	421	281	21	1.3	0.9	13.0	0.001L	0.0003L	0.005L	0.676	0.279
3	677	445	41	0.6	0.2	6.5	0.0002L	0.00006L	0.002L	0.677	0.281

Table A2 Details of the computational mesh grid for actuated flow ($f^* = 8.0$, $a^* = 0.001$, $X_0 = 0.9$)

Grid	N_{ξ}	N_{η}	N_{ζ}	$\delta \xi_{ m min}^+$	$\delta\eta_{ m min}^+$	$\delta\zeta_{ m min}^+$	$\Delta l_{\xi}^{ ext{min}}$	$\Delta l_{\eta}^{ m min}$	$\Delta l_{\zeta}^{ m min}$	C_L	C_D
1	213	141	13	2.0	1.4	21.7	0.008L	0.0006L	0.008L	0.95	0.110
2	421	281	21	1.3	0.9	13.0	0.001L	0.0003L	0.005L	0.89	0.090
3	677	445	41	0.6	0.2	6.5	0.0002L	0.00006L	0.002L	0.90	0.090

 ζ are represented by N_{ξ} , N_{η} , and N_{ζ} , respectively. The wall unit spacings along the ξ , η , and ζ directions are represented by $\delta \xi_{\min}^+$, $\delta\eta_{\min}^+$, and $\delta\zeta_{\min}^+$, respectively. The minimum grid spacings along the ξ , η , and ζ directions are represented by Δl_{ξ}^{\min} , Δl_{η}^{\min} , and Δl_{ζ}^{\min} in the tables (Tables A1 and A2), respectively. The minimum grid spacings were chosen to ensure that η^+ < 1.0 in order to accurately resolve the boundary layer along the airfoil surface. The boundary conditions and time step are kept constant for all grids: the same as those reported in Sec. II. Grid 3 has the highest grid refinement (i.e., highest grid resolution) in the three directions (ξ, η, ζ) . The mesh domain of grid 2 and a zoomed-in view with the airfoil are shown in Fig. 1. As can be seen from Table A1, the C_L and C_D results of the unactuated flows obtained from the three grids were similar because the deviations between the C_L and C_D results of grids 1 and 2, as compared to grid 3, were about 0.5%. From Table A2, the results of C_L and C_D of the actuated flow were similar. The percentage difference of C_L and C_D results of the actuated flow of grid 1, as compared to grid 3, were about 5 and 2%, respectively. The percentage difference of C_L between grid 2 and grid 3 reduced to about 1%, whereas C_D of grid 2 is the same as that of grid 3. These show that the results are grid independent, and grid 2 is suitable to obtain grid-independent results for our simulations. As a result, therefore, grid 2 was selected to perform the simulations for this study.

Figure A1 shows a log-log plot of the C_L error and the grid spacing in the η direction. The C_L error is calculated by the absolute difference between the C_L of grid 1 and grid 2 as compared to grid 3; i.e., grid 3 was used as the exact solution. From Fig. A1, the slope of the

log-log plot is 1.98; i.e., the order of numerical accuracy is two. This verifies that the numerical scheme adopted in this study is second-order accurate.

Acknowledgments

This work was supported by the National Science Foundation grant CBET 1905355. The computational resources were provided by the High Performance Research Computing facilities at Texas A&M University.

References

- [1] Carmichael, B. H., "Low Reynolds Number Airfoil Survey, Volume 1," NASA CR 165803, 1981, https://ntrs.nasa.gov/citations/19820006186
 [retrieved 15 Sept. 2022].
- [2] Mueller, T. J., and DeLaurier, J. D., "Aerodynamics of Small Vehicles," Annual Review of Fluid Mechanics, Vol. 35, No. 1, 2003, pp. 89–111. https://doi.org/10.1146/annurev.fluid.35.101101.161102
- [3] Francis, M. S., "Unmanned Air Systems: Challenge and Opportunity," Journal of Aircraft, Vol. 49, No. 6, 2012, pp. 1652–1665. https://doi.org/10.2514/1.C031425
- [4] Mueller, T. J., and Batill, S. M., "Experimental Studies of Separation on a Two-Dimensional Airfoil at Low Reynolds Numbers," *AIAA Journal*, Vol. 20, No. 4, 1982, pp. 457–463. https://doi.org/10.2514/3.51095
- [5] Lissaman, P., "Low-Reynolds-Number Airfoils," *Annual Review of Fluid Mechanics*, Vol. 15, No. 1, 1983, pp. 223–239. https://doi.org/10.1146/annurev.fl.15.010183.001255

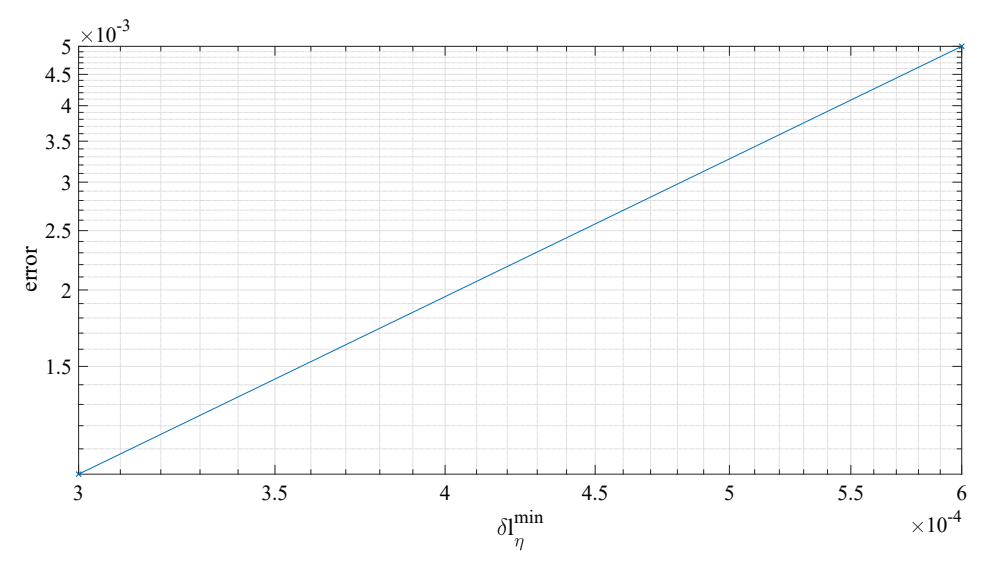


Fig. A1 Order of accuracy of grid convergence study. The absolute error of lift coefficient C_L of unactuated airfoil at AOA = 15 deg plotted against the minimum grid spacing along η direction in log-log scale.

- [6] Jones, G., Santer, M., Debiasi, M., and Papadakis, G., "Control of Flow Separation Around an Airfoil at Low Reynolds Numbers Using Periodic Surface Morphing," *Journal of Fluids and Structures*, Vol. 76, Jan. 2018, pp. 536–557. https://doi.org/10.1016/j.jfluidstructs.2017.11.008
- [7] Gad-el Hak, M., Flow Control: Passive, Active, and Reactive Flow Management, Cambridge Univ. Press, Cambridge, England, U.K., 2000, pp. 150–188. https://doi.org/10.1017/CBO9780511529535
- [8] Seifert, A., Darabi, A., and Wyganski, I., "Delay of Airfoil Stall by Periodic Excitation," *Journal of Aircraft*, Vol. 33, No. 4, 1996, pp. 691–698. https://doi.org/10.2514/3.47003
- [9] Wu, J.-Z., Lu, X.-Y., Denny, A. G., Fan, M., and Wu, J.-M., "Post-Stall Flow Control on an Airfoil by Local Unsteady Forcing," *Journal of Fluid Mechanics*, Vol. 371, Sept. 1998, pp. 21–58. https://doi.org/10.1017/s0022112098002055
- [10] Glezer, A., and Amitay, M., "Synthetic Jets," Annual Review of Fluid Mechanics, Vol. 34, No. 1, 2002, pp. 503–529. https://doi.org/10.1146/annurev.fluid.34.090501.094913
- [11] Amitay, M., Smith, D. R., Kibens, V., Parekh, D. E., and Glezer, A., "Aerodynamic Flow Control over an Unconventional Airfoil Using Synthetic Jet Actuators," *AIAA Journal*, Vol. 39, No. 3, 2001, pp. 361–370. https://doi.org/10.2514/2.1323
- [12] Buchmann, N. A., Atkinson, C., and Soria, J., "Influence of ZNMF Jet Flow Control on the Spatio-Temporal Flow Structure over a NACA-0015 Airfoil," *Experiments in Fluids*, Vol. 54, No. 3, 2013, Paper 1485. https://doi.org/10.1007/s00348-013-1485-7
- [13] Zhou, Y., and Wang, Z., "Effects of Surface Roughness on Separated and Transitional Flows over a Wing," AIAA Journal, Vol. 50, No. 3, 2012, pp. 593–609. https://doi.org/10.2514/1.J051237
- [14] Lin, J. C., "Review of Research on Low-Profile Vortex Generators to Control Boundary-Layer Separation," *Progress in Aerospace Sciences*, Vol. 38, Nos. 4–5, 2002, pp. 389–420. https://doi.org/10.1016/S0376-0421(02)00010-6
- [15] Manolesos, M., and Voutsinas, S. G., "Experimental Investigation of the Flow Past Passive Vortex Generators on an Airfoil Experiencing Three-Dimensional Separation," *Journal of Wind Engineering and Industrial Aerodynamics*, Vol. 142, July 2015, pp. 130–148. https://doi.org/10.1016/j.jweia.2015.03.020
- [16] Greenblatt, D., and Wygnanski, I. J., "The Control of Flow Separation by Periodic Excitation," *Progress in Aerospace Sciences*, Vol. 36, No. 7, 2000, pp. 487–545. https://doi.org/10.1016/S0376-0421(00)00008-7
- [17] Munday, D., and Jacob, J., "Active Control of Separation on a Wing with Oscillating Camber," *Journal of Aircraft*, Vol. 39, No. 1, 2002, pp. 187–189. https://doi.org/10.2514/2.2915
- [18] Jones, G., Santer, M., and Papadakis, G., "Control of Low Reynolds Number Flow Around an Airfoil Using Periodic Surface Morphing: A Numerical Study," *Journal of Fluids and Structures*, Vol. 76, Jan. 2018, pp. 95–115. https://doi.org/10.1016/j.jfluidstructs.2017.09.009
- [19] Rodriguez, I., Lehmkuhl, O., and Borrell, R., "Effects of the Actuation on the Boundary Layer of an Airfoil at Reynolds Number Re = 60000," Flow, Turbulence and Combustion, Vol. 105, No. 2, May 2020, pp. 607– 626. https://doi.org/10.1007/s10494-020-00160-y
- [20] Glezer, A., "Some Aspects of Aerodynamic Flow Control Using Synthetic-Jet Actuation," *Philosophical Transactions of the Royal Society of London, Series A: Mathematical, Physical and Engineering Sciences*, Vol. 369, No. 1940, 2011, pp. 1476–1494. https://doi.org/10.1098/rsta.2010.0374
- [21] Hsiao, F.-B., Liu, C.-F., and Shyu, J.-Y., "Control of Wall-Separated Flow by Internal Acoustic Excitation," *AIAA Journal*, Vol. 28, No. 8, 1990, pp. 1440–1446. https://doi.org/10.2514/3.25236
- [22] Schubauer, G. B., and Skramstad, H. K., "Laminar Boundary-Layer Oscillations and Transition on a Flat Plate," *Journal of Research of the National Bureau of Standard*, Vol. 38, Feb. 1947, pp. 251–292. https://doi.org/10.6028/jres.038.013
- [23] Seifert, A., Eliahu, S., Greenblatt, D., and Wygnanski, I., "Use of Piezoelectric Actuators for Airfoil Separation Control," *AIAA Journal*, Vol. 36, No. 8, 1998, pp. 1535–1537. https://doi.org/10.2514/2.549
- [24] Mathew, J., Song, Q., Sankar, B. V., Sheplak, M., and Cattafesta, L. N., III, "Optimized Design of Piezoelectric Flap Actuators for Active Flow

- Control," *AIAA Journal*, Vol. 44, No. 12, 2006, pp. 2919–2928. https://doi.org/10.2514/1.19409
- [25] Munday, D., and Jacob, J., "Active Control of Separation on a Wing with Oscillating Camber," *Journal of Aircraft*, Vol. 39, No. 1, 2002, pp. 187–189. https://doi.org/10.2514/2.2915
- [26] Di, G., Wu, Z., and Huang, D., "The Research on Active Flow Control Method with Vibration Diaphragm on a NACA0012 Airfoil at Different Stalled Angles of Attack," *Aerospace Science and Technology*, Vol. 69, Oct. 2017, pp. 76–86. https://doi.org/10.1016/j.ast.2017.06.020
- [27] Bani-Hani, M. A., and Karami, M. A., "Analytical Structural Optimization and Experimental Verifications for Traveling Wave Generation in Self-Assembling Swimming Smart Boxes," Smart Materials and Structures, Vol. 24, No. 9, 2015, Paper 094005. https://doi.org/10.1088/0964-1726/24/9/094005
- [28] Gillis, G. B., "Undulatory Locomotion in Elongate Aquatic Vertebrates: Anguilliform Swimming Since Sir James Gray," *American Zoologist*, Vol. 36, No. 6, 1996, pp. 656–665. https://doi.org/10.1093/icb/36.6.656
- [29] Borazjani, I., "Hydrodynamics of Aquatic Swimming: Inspiration for Flow Control," *Bioinspiration, Biomimetics, and Bioreplication XI*, Vol. 11586, International Soc. for Optics and Photonics, Bellingham, WA, 2021, Paper 115860. https://doi.org/10.1117/12.2582426
- [30] Taylor, G., Triantafyllou, M. S., and Tropea, C., Animal Locomotion, Springer Science and Business Media, Cham, Switzerland, 2010, pp. 1– 443. https://doi.org/10.1007/978-3-642-11633-9
- [31] Anderson, E. J., Megillis, W. R., and Grosenbaugh, M. A., "The Boundary Layer of Swimming Fish," *Journal of Experimental Biology*, Vol. 204, No. 1, 2001, pp. 81–102. https://doi.org/10.1242/jeb.204.1.81
- [32] Borazjani, I., and Sotiropoulos, F., "Numerical Investigation of the Hydrodynamics of Anguilliform Swimming in the Transitional and Inertial Flow Regimes," *Journal of Experimental Biology*, Vol. 212, No. 4, 2009, pp. 576–592. https://doi.org/10.1242/jeb.025007
- [33] Akbarzadeh, A., and Borazjani, I., "Controlling Flow Separation on a Thick Airfoil Using Backward Traveling Waves," AIAA Journal, Vol. 58, No. 9, 2020, pp. 3799–3807. https://doi.org/10.2514/1.J059428
- [34] Akbarzadeh, A., and Borazjani, I., "Reducing Flow Separation of an Inclined Plate via Travelling Waves," *Journal of Fluid Mechanics*, Vol. 880, Dec. 2019, pp. 831–863. https://doi.org/10.1017/jfm.2019.705
- [35] Lighthill, M. J., "Note on the Swimming of Slender Fish," *Journal of Fluid Mechanics*, Vol. 9, No. 2, 1960, p. 305–317. https://doi.org/10.1017/S0022112060001110
- [36] Akbarzadeh, A. M., and Borazjani, I., "Large Eddy Simulations of a Turbulent Channel Flow with a Deforming Wall Undergoing High Steepness Traveling Waves," *Physics of Fluids*, Vol. 31, No. 12, 2019, Paper 125107. https://doi.org/10.1063/1.5131268
- [37] Akbarzadeh, A., and Borazjani, I., "A Numerical Study on Controlling Flow Separation via Surface Morphing in the Form of Backward Traveling Waves," AIAA Aviation 2019 Forum, AIAA Paper 2019-3589, 2019. https://doi.org/10.2514/6.2019-3589
- [38] Olivett, A., Corrao, P., and Karami, M., "Flow Control and Separation Delay in Morphing Wing Aircraft Using Traveling Wave Actuation," Smart Materials, Adaptive Structures and Intelligent Systems, Vol. 84027, American Soc. of Mechanical Engineers Paper SMA-SIS2020-2355, 2020, p. V001T06A009. https://doi.org/10.1115/SMASIS2020-2355
- [39] Olivett, A., Corrao, P., and Karami, M. A., "Flow Control and Separation Delay in Morphing Wing Aircraft Using Traveling Wave Actuation," Smart Materials and Structures, Vol. 30, No. 2, 2021, Paper 025028. https://doi.org/10.1088/1361-665X/abd347
- [40] Ogunka, U., Akbarzadeh, A., and Borazjani, I., "The Role of Amplitude on Controlling Flow Separation Using Traveling Wave Morphing," *AIAA SciTech* 2021, AIAA Paper 2021-2005, 2021. https://doi.org/10.2514/6.2021-2005
- [41] Ogunka, U. E., Akbarzadeh, A., and Borazjani, I., "Flow Control with Traveling-Wave Surface Morphing at Post-Stall Angles of Attack," AIAA SciTech 2022 Forum, AIAA Paper 2022-1948, 2022. https://doi.org/10.2514/6.2022-1948
- [42] Ge, L., and Sotiropoulos, F., "A Numerical Method for Solving the 3D Unsteady Incompressible Navier–Stokes Equations in Curvilinear

- Domains with Complex Immersed Boundaries," *Journal of Computational Physics*, Vol. 225, No. 2, 2007, pp. 1782–1809. https://doi.org/10.1016/j.jcp.2007.02.017
- [43] Borazjani, I., Ge, L., and Sotiropoulos, F., "Curvilinear Immersed Boundary Method for Simulating Fluid Structure Interaction with Complex 3D Rigid Bodies," *Journal of Computational Physics*, Vol. 227, No. 16, 2008, pp. 7587–7620. https://doi.org/10.1016/j.jcp.2008.04.028
- [44] Asgharzadeh, H., and Borazjani, I., "A Newton-Krylov Method with an Approximate Analytical Jacobian for Implicit Solution of Navier-Stokes Equations on Staggered Overset-Curvilinear Grids with Immersed Boundaries," *Journal of Computational Physics*, Vol. 331, Feb. 2017, pp. 227–256. https://doi.org/10.1016/j.jcp.2016.11.033
- [45] Borazjani, I., and Akbarzadeh, A., "Large Eddy Simulations of Flows with Moving Boundaries," *Modeling and Simulation of Turbulent Mix*ing and Reaction, Springer, Berlin, 2020, pp. 201–225. https://doi.org/10.1007/978-981-15-2643-5_9
- [46] Asadi, H., Asgharzadeh, H., and Borazjani, I., "On the Scaling of Propagation of Periodically Generated Vortex Rings," *Journal of Fluid Mechanics*, Vol. 853, Aug. 2018, pp. 150–170. https://doi.org/10.1017/jfm.2018.529
- [47] Ogunka, U. E., Daghooghi, M., Akbarzadeh, A. M., and Borazjani, I., "The Ground Effect in Anguilliform Swimming," *Biomimetics*, Vol. 5, No. 1, 2020, Paper 9. https://doi.org/10.3390/biomimetics5010009
- [48] Bottom, R., II, Borazjani, I., Blevins, E., and Lauder, G., "Hydrodynamics of Swimming in Stingrays: Numerical Simulations and the Role of the Leading-Edge Vortex," *Journal of Fluid Mechanics*, Vol. 788, Jan. 2016, pp. 407–443. https://doi.org/10.1017/jfm.2015.702
- [49] Daghooghi, M., and Borazjani, I., "Self-Propelled Swimming Simulations of Bio-Inspired Smart Structures," *Bioinspiration and Biomimetics*, Vol. 11, No. 5, 2016, Paper 056001. https://doi.org/10.1088/1748-3190/11/5/056001
- [50] Borazjani, I., "Fluid–Structure Interaction, Immersed Boundary-Finite Element Method Simulations of Bio-Prosthetic Heart Valves," Computer Methods in Applied Mechanics and Engineering, Vol. 257, April 2013, pp. 103–116. https://doi.org/10.1016/j.cma.2013.01.010
- [51] Hedayat, M., and Borazjani, I., "Comparison of Platelet Activation Through Hinge vs Bulk Flow in Bileaflet Mechanical Heart Valves," *Journal of Biomechanics*, Vol. 83, Jan. 2019, pp. 280–290. https://doi.org/10.1016/j.jbiomech.2018.12.003
- [52] Hedayat, M., Asgharzadeh, H., and Borazjani, I., "Platelet Activation of Mechanical Versus Bioprosthetic Heart Valves During Systole," *Journal* of Biomechanics, Vol. 56, May 2017, pp. 111–116. https://doi.org/10.1016/j.jbiomech.2017.03.002
- [53] Asgharzadeh, H., Asadi, H., Meng, H., and Borazjani, I., "A Non-Dimensional Parameter for Classification of the Flow in Intracranial Aneurysms. II. Patient-Specific Geometries," *Physics of Fluids*, Vol. 31, No. 3, 2019, Paper 031905. https://doi.org/10.1063/1.5081451
- [54] Asgharzadeh, H., and Borazjani, I., "A Non-Dimensional Parameter for Classification of the Flow in Intracranial Aneurysms. I. Simplified Geometries," *Physics of Fluids*, Vol. 31, No. 3, 2019, Paper 031904. https://doi.org/10.1063/1.5033942
- [55] Germano, M., Piomelli, U., Moin, P., and Cabot, W. H., "A Dynamic Subgrid-Scale Eddy Viscosity Model," *Physics of Fluids A: Fluid Dynamics*, Vol. 3, No. 7, 1991, pp. 1760–1765. https://doi.org/10.1063/1.857955
- [56] Rizzetta, D. P., Visbal, M. R., and Morgan, P. E., "A High-Order Compact Finite-Difference Scheme for Large-Eddy Simulation of Active Flow Control," *Progress in Aerospace Sciences*, Vol. 44, No. 6, 2008, pp. 397–426. https://doi.org/10.1016/j.paerosci.2008.06.003
- [57] Akhavan-Safaei, A., Seyedi, S. H., and Zayernouri, M., "Anomalous Features in Internal Cylinder Flow Instabilities Subject to Uncertain Rotational Effects," *Physics of Fluids*, Vol. 32, No. 9, 2020, Paper 094107. https://doi.org/10.1063/5.0021815
- [58] Celik, I., Cehreli, Z., and Yavuz, I., "Index of Resolution Quality for Large Eddy Simulations," *Journal of Fluids Engineering*, Vol. 127, No. 5, 2005, pp. 949–958. https://doi.org/10.1115/1.1990201
- [59] Esfahani, A., Webb, N., and Samimy, M., "Flow Separation Control over a Thin Post-Stall Airfoil: Effects of Excitation Frequency," *AIAA Journal*, Vol. 57, No. 5, 2019, pp. 1826–1838. https://doi.org/10.2514/1.J057796

- [60] Hunt, J. C. R., Wray, A. A., and Moin, P., "Eddies, Streams, and Convergence Zones in Turbulent Flows," Studying Turbulence Using Numerical Simulation Databases, 2. Proceedings of the 1988 Summer Program, Center for Turbulence Research, NASA CP 19890015 184, 1988, pp. 193–208, https://ntrs.nasa.gov/citations/19890015184 [retrieved 2 Aug. 2022].
- [61] Ogunka, U. E., Akbarzadeh, A. M., and Borazjani, I., "Video: Stall Delay of a NACA0018 Airfoil by Traveling Wave Actuations," 74th Annual Meeting of the APS Division of Fluid Dynamics—Gallery of Fluid Motion, American Physical Soc., Phoenix, Arizona, 2021. https://doi.org/10.1103/aps.dfd.2021.gfm.v0092
- [62] Lei, J., Zhang, J., and Niu, J., "Effect of Active Oscillation of Local Surface on the Performance of Low Reynolds Number Airfoil," Aerospace Science and Technology, Vol. 99, April 2020, Paper 105774. https://doi.org/10.1016/j.ast.2020.105774
- [63] Kang, W., Lei, P., Zhang, J., and Xu, M., "Effects of Local Oscillation of Airfoil Surface on Lift Enhancement at Low Reynolds Number," *Journal of Fluids and Structures*, Vol. 57, Aug. 2015, pp. 49–65. https://doi.org/10.1016/j.jfluidstructs.2015.05.009
- [64] Kotapati, R. B., Mittal, R., Marxen, O., Ham, F., You, D., and Cattafesta, L. N., "Nonlinear Dynamics and Synthetic-Jet-Based Control of a Canonical Separated Flow," *Journal of Fluid Mechanics*, Vol. 654, May 2010, pp. 65–97. https://doi.org/10.1017/s002211201000042x
- [65] Feero, M. A., Lavoie, P., and Sullivan, P. E., "Influence of Synthetic Jet Location on Active Control of an Airfoil at Low Reynolds Number," *Experiments in Fluids*, Vol. 58, No. 8, 2017, pp. 1–12. https://doi.org/10.1007/s00348-017-2387-x
- [66] Donovan, J., Kral, L., and Cary, A., "Active Flow Control Applied to an Airfoil," 36th AIAA Aerospace Sciences Meeting and Exhibit, AIAA Paper 1998-0210, 1998. https://doi.org/10.2514/6.1998-210
- [67] Yarusevych, S., Sullivan, P. E., and Kawall, J. G., "On Vortex Shedding from an Airfoil in Low-Reynolds-Number Flows," *Journal of Fluid Mechanics*, Vol. 632, Aug. 2009, pp. 245–271. https://doi.org/10.1017/S0022112009007058
- [68] Nonomura, T., Aono, H., Sato, M., Yakeno, A., Okada, K., Abe, Y., and Fujii, K., "Control Mechanism of Plasma Actuator for Separated Flow Around NACA0015 at Reynolds Number 63,000-Separation Bubble Related Mechanisms," 51st AIAA Aerospace Sciences Meeting Including the New Horizons Forum and Aerospace Exposition, AIAA Paper 2013-0853, 2013. https://doi.org/10.2514/6.2013-853
- [69] Sato, M., Nonomura, T., Okada, K., Asada, K., Aono, H., Yakeno, A., Abe, Y., and Fujii, K., "Mechanisms for Laminar Separated-Flow Control Using Dielectric-Barrier-Discharge Plasma Actuator at Low Reynolds Number," *Physics of Fluids*, Vol. 27, No. 11, 2015, Paper 117101. https://doi.org/10.1063/1.4935357
- [70] Sato, M., Okada, K., Asada, K., Aono, H., Nonomura, T., and Fujii, K., "Unified Mechanisms for Separation Control Around Airfoil Using Plasma Actuator with Burst Actuation Over Reynolds Number Range of 103–106," *Physics of Fluids*, Vol. 32, No. 2, 2020, Paper 025102. https://doi.org/10.1063/1.5136072
- [71] Aono, H., Kawai, S., Nonomura, T., Sato, M., Fujii, K., and Okada, K., "Plasma-Actuator Burst-Mode Frequency Effects on Leading-Edge Flow-Separation Control at Reynolds Number 2.6 × 10 5," AIAA Journal, Vol. 55, No. 11, 2017, pp. 3789–3806. https://doi.org/10.2514/1.J055727
- [72] Sato, M., Asada, K., Nonomura, T., Aono, H., Yakeno, A., and Fujii, K., "Mechanisms for Turbulent Separation Control Using Plasma Actuator at Reynolds Number of 1.6 × 106," *Physics of Fluids*, Vol. 31, No. 9, 2019, Paper 095107. https://doi.org/10.1063/1.5110451
- [73] Gad-el Hak, M., "The Taming of the Shrew: Why is it so Difficult to Control Turbulence?" *Active Flow Control*, Springer, Berlin, 2007, pp. 1–24. https://doi.org/10.1007/978-3-540-71439-2_1
- [74] Thompson, E., and Goza, A., "Surface Morphing for Aerodynamic Flows at Low and Stalled Angles of Attack," *Physical Review Fluids*, Vol. 7, No. 2, 2022, Paper 024703. https://doi.org/10.1103/PhysRevFluids.7.024703
- [75] Cleaver, D. J., Wang, Z., Gursul, I., and Visbal, M., "Lift Enhancement by Means of Small-Amplitude Airfoil Oscillations at Low Reynolds Numbers," AIAA Journal, Vol. 49, No. 9, 2011, pp. 2018–2033. https://doi.org/10.2514/1.J051014
- [76] Guowei, Y., Shanwu, W., Ningyu, L., and Lixian, Z., "Control of Unsteady Vortical Lift on an Airfoil by Leading-Edge Blowing-

- Suction," *Acta Mechanica Sinica*, Vol. 13, No. 4, 1997, pp. 304–312. https://doi.org/10.1007/BF02487189
- [77] Huang, L., Huang, P., LeBeau, R., and Hauser, T., "Numerical Study of Blowing and Suction Control Mechanism on NACA0012 Airfoil," *Journal of Aircraft*, Vol. 41, No. 5, 2004, pp. 1005–1013. https://doi.org/10.2514/1.2255
- [78] Post, M. L., and Corke, T. C., "Separation Control on High Angle of Attack Airfoil Using Plasma Actuators," *AIAA Journal*, Vol. 42, No. 11, 2004, pp. 2177–2184. https://doi.org/10.2514/1.2929
- [79] Sato, M., Aono, H., Yakeno, A., Nonomura, T., Fujii, K., Okada, K., and Asada, K., "Multifactorial Effects of Operating Conditions of Dielectric-Barrier-Discharge Plasma Actuator on Laminar-Separated-Flow Control," AIAA Journal, Vol. 53, No. 9, 2015, pp. 2544–2559. https://doi.org/10.2514/1.J053700
- [80] Mitchell, A. M., Barberis, D., Molton, P., and Delery, J., "Control of Leading-Edge Vortex Breakdown by Trailing Edge Injection," *Journal* of Aircraft, Vol. 39, No. 2, 2002, pp. 221–226. https://doi.org/10.2514/2.2942
- [81] Bradley, R., and Wray, W., "A Conceptual Study of Leading-Edge-Vortex Enhancement by Blowing," *Journal of Aircraft*, Vol. 11, No. 1, 1974, pp. 33–38. https://doi.org/10.2514/3.60318
- [82] Mitchell, A. M., Barberis, D., Molton, P., and Delery, J., "Oscillation of Vortex Breakdown Location and Blowing Control of Time-Averaged

- Location," AIAA Journal, Vol. 38, No. 5, 2000, pp. 793–803. https://doi.org/10.2514/2.1059
- [83] Hong, J. S., Celik, Z. Z., and Roberts, L., "Effects of Leading-Edge Lateral Blowing on Delta Wing Aerodynamics," AIAA Journal, Vol. 34, No. 12, 1996, pp. 2471–2478. https://doi.org/10.2514/3.13426
- [84] Wang, Z.-J., Jiang, P., and Gursul, I., "Effect of Thrust-Vectoring Jets on Delta Wing Aerodynamics," *Journal of Aircraft*, Vol. 44, No. 6, 2007, pp. 1877–1888.
 - https://doi.org/10.2514/1.30568
- [85] McCormick, S., and Gursul, I., "Effect of Shear-Layer Control on Leading-Edge Vortices," *Journal of Aircraft*, Vol. 33, No. 6, 1996, pp. 1087–1093. https://doi.org/10.2514/3.47061
- [86] Gursul, I., Wang, Z., and Vardaki, E., "Review of Flow Control Mechanisms of Leading-Edge Vortices," *Progress in Aerospace Sciences*, Vol. 43, Nos. 7–8, 2007, pp. 246–270. https://doi.org/10.1016/j.paerosci.2007.08.001
- [87] Chen, C., Seele, R., and Wygnanski, I., "Flow Control on a Thick Airfoil Using Suction Compared to Blowing," *AIAA Journal*, Vol. 51, No. 6, 2013, pp. 1462–1472. https://doi.org/10.2514/1.J052098

P. G. Tucker Associate Editor